

1 **Alluvial architecture of mid-channel fluvial–tidal barforms: The mesotidal**  
2 **Lower Columbia River, Oregon/Washington, USA**

3  
4 Prokocki, E.W.<sup>1,\*</sup>, Best, J.L.<sup>1,2</sup>, Ashworth, P.J.<sup>3</sup>, Sambrook Smith, G.H.<sup>4</sup>, Nicholas, A.P.<sup>5</sup>,  
5 Parsons, D.R.<sup>6</sup>, Simpson, C.J.<sup>7</sup>

6  
7 <sup>1</sup>Department of Geology, University of Illinois, 1301 West Green Street, Urbana, IL 61801, USA  
8 \*now at: Jackson School of Geosciences, 2305 Speedway Stop C1160, Austin, TX 78712, USA  
9 (Email: ewaschle2@gmail.com)

10 <sup>2</sup>Departments of Geography & GIS, Mechanical Science and Engineering, and Ven Te Chow  
11 Hydrosystems Laboratory, University of Illinois, 1301 West Green Street, Urbana, IL 61801,  
12 USA

13 <sup>3</sup>Division of Geography and Geology, School of Environment and Technology, University of  
14 Brighton, Brighton, Sussex BN2 4GJ, UK

15 <sup>4</sup>School of Geography, Earth, Environmental Sciences, University of Birmingham, Edgbaston,  
16 Birmingham, B15 2TT, UK

17 <sup>5</sup>Department of Geography, College of Life and Environmental Sciences, University of Exeter,  
18 EX4 4RJ, UK

19 <sup>6</sup>Department of Geography, Environment and Earth Sciences, Faculty of Science and  
20 Engineering, University of Hull, Hull, HU6 7RX, UK

21 <sup>7</sup>Fulcrum Graphic Communications Inc., Airdrie, Alberta, Canada

22  
23  
24 **Associate Editor – Charlie Bristow**

25  
26 **Short title: Fluvio-tidal barform architecture and sedimentology**

27  
28 **ABSTRACT**

29 Barforms of mesotidal to macrotidal fluvial–tidal transitions, regardless of fluvial-discharge, are  
30 currently thought to display a sedimentary architecture dominated by tidal signatures. Due to the  
31 scarcity of observations from modern mesotidal fluvial–tidal transitions, especially those of  
32 multi-channelled large-rivers (mean annual discharge  $\geq 7000 \text{ m}^3 \text{ s}^{-1}$  and peak discharges  $\geq 15,000$   
33  $\text{m}^3 \text{ s}^{-1}$ ) with mid-channel bars, this concept remains unproven. The present study analyses data  
34 produced by a combination of high-resolution ground penetrating radar and coupled shallow  
35 vibracores ( $< 5 \text{ m}$  depth), collected from modern fluvial–tidal mid-channel bars of the mesotidal  
36 multi-channelled Lower Columbia River, Washington/Oregon, USA, which experiences peak

37 discharges  $\geq 18,000 \text{ m}^3 \text{ s}^{-1}$ . These data were used alongside time-sequenced aerial imagery to  
38 characterize the spatio-temporal sedimentological evolution of these barforms in singular flows  
39 or combined flows consisting of river, tidal and/or wind-wave oscillatory, current components  
40 operating in unique fluvial–tidal transition regimes. Results indicate that *ca* 75% of the Lower  
41 Columbia River fluvial–tidal transition produces braid-bars with basal to bar-top  
42 sedimentological architectures that are indistinguishable from fluvial-only braid-bars recorded in  
43 the literature. Barform stratal characteristics within the fluvial–tidal transitions of mesotidal  
44 large-rivers are therefore more likely to be dominated by downstream-oriented currents.  
45 Furthermore, a new style of low-angle ( $<5^\circ$ ) inclined heterolithic stratification found in bar-top  
46 accretion-sets within upper-mixed tidal–fluvial regime braid-bars is observed. This common  
47 stratification is created by combined-flows characterized by intrabasinal wind-wave oscillatory-  
48 currents and bidirectional tidal-currents. This inclined heterolithic stratification marks the initial  
49 downstream fluvial–tidal crossover point from Lower Columbia River up-dip fully-fluvial braid-  
50 bar architectures, to those possessing bar-top facies produced by the hydraulic-sedimentation  
51 response of combined intrabasinal wind-wave and tidal influence. When preserved, this form of  
52 mid-channel bar inclined heterolithic stratification provides a unique sedimentological signature  
53 of multi-channelled fluvial–tidal transitions that possess an open-water lower basin with  
54 intrabasinal wind-waves.

55

56 **Keywords: Fluvial-tidal bars, Inclined Heterolithic Stratification, intrabasinal wind-waves,**  
57 **Lower Columbia River**

58

59

60 **(A) INTRODUCTION**

61 Fluvial–tidal transitions (FTTs) or fluvial–tidal zones (van den Berg *et al.*, 2007), are one of the  
62 most complex multi-thread to single-thread channelized settings on Earth (Dalrymple & Choi,  
63 2007). Depending on channel-bed slope and tidal range, FTTs may extend tens to hundreds of  
64 river kilometres (rkm) landward from river mouths to the landward most point of measurable  
65 tidally-induced variations of the low-river stage water surface or tidal-limit (Dalrymple & Choi,  
66 2007; Hoitink & Jay, 2016). Thus, FTTs span several unique settings from lower estuaries, or  
67 deltas, where salt-wedge intrusion occurs, to the brackish-water upper estuary, or delta, and  
68 through the freshwater tidal river reach (cf. Dalrymple & Choi, 2007; Hoitink & Jay, 2016).

69 Fluvial–tidal transitions are combined-flow environments characterized by the interplay between  
70 bidirectional tidal-flows, unidirectional river-currents, oceanic to intrabasinal wind-waves, and  
71 density-driven vorticity generated by saltwater intrusion (Dalrymple & Choi, 2007). By  
72 evaluating either the mean ratio of hypothesized (Dalrymple *et al.*, 2015), or measured (Jay *et al.*,  
73 1990; Losada *et al.*, 2017), tidal-energy *versus* fluvial-energy input, three general hydraulic  
74 zones describe FTTs (cf. Jay *et al.*, 1990; Hoitink & Jay, 2016; Jablonski & Dalrymple, 2016):  
75 (i) marine to tidally-dominated lower estuary, or delta; (ii) tidally-dominated, fluvially-  
76 influenced or mixed tidal-fluvial regime (upper estuary, or delta, to lower tidal river reach); and  
77 (iii) fluvially-dominated, tidally-influenced regime (mid to upper-tidal river reach). The  
78 longitudinal boundaries of these regimes, however, fluctuate in space and time due to the  
79 interactions between spring to neap tidal-cycles and varying river-stages (Dalrymple & Choi,  
80 2007; Dalrymple *et al.*, 2015). This classification scheme does, however, exclude the effects of  
81 oceanic-waves within lower FTTs and intrabasinal wind-waves in mid to upper-FTTs, which can

82 be important hydraulic constituents in particular settings (cf. Chaumillon *et al.*, 2008; Peterson *et al.*, 2014; Prokocki *et al.*, 2015).

84 Point-bars or mid-channel bars (Hubbard *et al.*, 2011; Jablonski & Dalrymple, 2016;  
85 Leuven *et al.*, 2016; van de Lageweg & Feldman, 2018) may characterize FTTs, and their  
86 presence depends on whether the system is multi-channelled or single-threaded (Seminara *et al.*,  
87 2001). Due to the interplay between the dominant and subordinate fluvial–tidal currents, the  
88 sedimentology of FTT barforms is likely more complex than unidirectional-current fluvial bars  
89 (Dalrymple & Choi, 2007; van den Berg *et al.*, 2007; Martinius & van den Berg, 2011; van de  
90 Lageweg & Feldman, 2018). A widely adopted fluvial–tidal barform model suggests that in the  
91 downstream-direction there is a tendency for FTT barform accretion-sets to develop Inclined  
92 Heterolithic Stratification (IHS; Thomas *et al.*, 1987), where enhanced fine-grained deposition  
93 occurs during tidal-slackwater intervals and near the turbidity-maximum (TM; Fig. 1). This  
94 model, however, is limited in four respects. Firstly, its foundation rests upon a small number of  
95 modern studies (e.g. Smith 1987, 1989; Choi *et al.*, 2004; Dalrymple & Choi, 2007; Dalrymple  
96 *et al.*, 2012; Johnson & Dashtgard, 2014), whilst relying heavily on observations from ancient  
97 fluvial–tidal settings (e.g. Hubbard *et al.*, 2011; Fustic *et al.*, 2012; Feldman & Demko, 2015;  
98 Martinius *et al.*, 2015; Jablonski & Dalrymple, 2016), where the planform geometry, and  
99 hydraulic initial and boundary conditions, are not well-constrained. Secondly, it implies that IHS  
100 is strongly related to tidal-processes, and de-emphasizes the potential importance of fluvial and  
101 wind-wave processes (Smith *et al.*, 2009, 2011; Durkin *et al.*, 2015; Moreton & Carter, 2015) in  
102 producing IHS. Thirdly, it is conditioned upon single-thread FTTs with point-bars, and thus it is  
103 unknown whether the IHS model applies to multi-channelled FTTs with mid-channel bars.

104 Lastly, it portrays IHS trends from a longitudinal-viewpoint (upstream to downstream) and does  
105 not consider lateral variations.

106         Establishing whether contemporary FTT bars possess a sedimentological signature that  
107 can be unambiguously distinguished from purely marine and fluvial deposits is important for  
108 several reasons. Within sequence stratigraphic models, FTTs mark the landward extent of  
109 transgression and represent the basal flooding surfaces of highstand successions (Dalrymple *et*  
110 *al.*, 1992; Shanley *et al.*, 1992; Boyd *et al.*, 2006; Dalrymple & Choi, 2007). Knowledge of FTT  
111 stratal architecture is also beneficial to hydrocarbon exploration and production. For example,  
112 the Cretaceous bitumen-rich McMurray Formation, Alberta, Canada (Hein, 2015), is commonly  
113 interpreted as being constructed from FTT barform strata (Smith, 1988, 1989; Wightman &  
114 Pemberton, 1997; Wightman *et al.*, 1997; Hubbard *et al.*, 2011; Fustic *et al.*, 2012; Feldman &  
115 Demko, 2015; Martinius *et al.*, 2015; Jablonski & Dalrymple, 2016), but fully-fluvial McMurray  
116 Formation barform depositional models have also been proposed (cf. Moreton & Carter, 2015).  
117 Modern FTT barforms have thus received a lot of recent attention (Smith 1987, 1989; Smith *et*  
118 *al.*, 2009; Choi, 2010; Sisulak & Dashtgard, 2012; Choi *et al.*, 2013; Johnson & Dashtgard,  
119 2014; Carling *et al.*, 2015; Prokocki *et al.*, 2015; Leuven *et al.*, 2016) in order to establish how  
120 fluvial–tidal processes alter their morphology and alluvial architecture. Most sedimentological  
121 observations from modern FTTs, however, are restricted to bed-scale trenches and cores (e.g.  
122 Dalrymple & Rhodes, 1995; Choi *et al.*, 2004; van den Berg *et al.*, 2007; Baker *et al.*, 2010;  
123 Martinius & van den Berg, 2011; Sisulak & Dashtgard, 2012; Peterson *et al.*, 2014; Carling *et*  
124 *al.*, 2015; Prokocki *et al.*, 2015; Ghinassi *et al.*, 2018), whilst seismic data of bar-scale  
125 architecture is scarce, limited in its spatial resolution and confined to individual sandbanks, or  
126 sandbars (Chaumillon *et al.*, 2008, 2013). Thus, while abundant bar-scale seismic data exists for

127 ancient tide-dominated offshore deposits (Berné *et al.*, 2002) and fluvio-tidal systems (Hubbard  
128 *et al.*, 2011; Reijnenstein *et al.*, 2011), comparable data from modern FTT barforms is limited.

129 To address this data deficiency, the present study presents an integrated ground  
130 penetrating radar (GPR) and shallow (<5 m depth) vibrocore dataset collected in 2011 and 2013  
131 from FTT mid-channel bars of the mesotidal sand-bed, Lower Columbia River (LCR), USA (Fig.  
132 2A to D). Three primary questions are addressed herein:

- 133 1) What is the sedimentological architecture of large-river mid-channel bars within the  
134 mixed tidal–fluvial to fluvially-dominated, tidally-influenced FTT hydraulic regimes?
- 135 2) How does potential IHS within FTT mid-channel bar alluvial successions relate to: (i) bar  
136 migration rates and patterns; and (ii) varying contributions of combined-flow currents  
137 and associated depositional processes?
- 138 3) How similar, or different, is the sedimentary architecture of large-river FTT mid-channel  
139 bars relative to fluvial braid-bars?

140

## 141 **(A) STUDY REACH: LOWER COLUMBIA RIVER FLUVIAL–TIDAL TRANSITIONS**

### 142 **(B) Modern fluvial–tidal characteristics**

143 From the late 1800s to present, human-intervention within the Columbia River drainage basin  
144 has disrupted water and sediment supplies via irrigation depletion and dam closures, main  
145 navigation channel dredging and sand-mining, the installation of upriver permeable pile-dykes  
146 along the navigation channel, and jetty and dyke construction at its mouth (Sherwood *et al.*,  
147 1990; Gelfenbaum *et al.*, 1999; Jay *et al.*, 2011; Naik & Jay, 2011; Templeton & Jay, 2013).

148 Within this context, the LCR (1970 to 2004) mean annual fluvial-discharge,  $Q_{Wavg}$ , at the  
149 Beaver (Port Westward) gauge station (upstream boundary of study reach) is *ca* 6780 m<sup>3</sup> s<sup>-1</sup> (Fig.

150 3A; Naik & Jay, 2011). High-river stage winter and spring freshet daily peak-flows,  $Q_{Wpeak}$ , are  
151 typically moderated by dam release to between 15,000 to 17,000  $m^3 s^{-1}$  (Fig. 3A; Gelfenbaum,  
152 1983; Naik & Jay, 2011; Simenstad *et al.*, 2011), but may exceed bankfull conditions (18,000 to  
153 24,000  $m^3 s^{-1}$ ) during extreme spring freshets (Sherwood *et al.*, 1990; Jay & Naik, 2011; Naik &  
154 Jay, 2011; ). The inferred channel-bed slope,  $S_c$ , of the LCR is equal to *ca*  $1.15 \times 10^{-5}$  (Hickson,  
155 1912) as determined from the Columbia River Datum (CRD) low-tide and low-river stage water  
156 surface slope (Fig. 3B). Over this gradient, the LCR experiences meso-tidal mixed diurnal and  
157 semidiurnal tides where the mean diurnal tidal prism is  $11.0 \times 10^8 m^3$  (Walton & Adams, 1976),  
158 and the mean range of tide (MN) and highest astronomical tide are 1.7 m and 3.6 m respectively  
159 at its mouth, and 2.0 m and 4.0 m near Astoria, OR, as the result of marginal tidal-funnelling  
160 (Fig. 3B; Fain *et al.*, 2001; Simenstad *et al.*, 2011). At low-river stage, the LCR maximum tidal-  
161 limit extends to *ca* rkm 235 (Fig. 3B; Bonneville Dam), but tidal-modulation of the water surface  
162 height decreases to  $<0.2$  m at Vancouver, WA (rkm 172; Kukulka & Jay, 2003), whilst  
163 observable current reversals extend to *ca* rkm 109 (Fig. 3B; Clark & Snyder, 1969). These tidal-  
164 characteristics are similar to other less human-influenced fluvio-tidal systems along the central  
165 Cascadia Margin, USA, whose tides originate from the same amphidromic point (Table 1).

166 The hydrographic ratio,  $H_g$ , which equals  $(Q_{tide}/Q_{Wavg}) \times 6 \text{ hrs}$  (*half a tidal cycle*),  
167 where  $Q_{tide}$  is the mean diurnal tidal prism, is a commonly used parameter (cf. Peterson *et al.*,  
168 1984) to compare the large-scale balance between tidal and fluvial energy input between  
169 differing fluvial-tidal systems, where an  $H_g > 10$  suggests tidal-dominance, and systems with an  
170  $H_g < 10$  are considered fluvially-dominated. With respect to the LCR, its  $H_g$  is equal to 7, and it  
171 is therefore fluvially dominant (Table 1). Further evidence for LCR fluvial dominance  
172 throughout the study reach comes from: (i) hydraulic surveys of Jay (1984) that were conducted

173 over multiple tidal-cycles and low to high river stages (Fig. 4A); and (ii) LCR numerical  
174 modelling results (cf. Hamilton, 1990; Sandbach *et al.*, 2018). By computing the dissipation of  
175 potential tidal versus fluvial energy across modern LCR channel cross-sections (cf. Jay, 1984),  
176 Jay *et al.* (1990) divided the FTT (*ca* rkm 0 to 235) into three hydraulic reaches (Figs 3B and  
177 4A). (1) The most downstream reach is the tidally-dominated regime (TDR) spanning *ca* rkm 0  
178 to 21 that, during both low and high river flows, is characterized by strong bidirectional tidal-  
179 currents, saltwater intrusion, development of a TM, and oceanic-derived waves at its seaward  
180 end (cf. Fox *et al.*, 1984; Sherwood & Creager, 1990; Figs 3B and 4A). (2) The mixed tidal-  
181 fluvial regime (MTFR) extends from *ca* rkm 21 to 56, where fluvial-currents are dominant as the  
182 result of moderate to high river stages (Fig. 4A). At low-river stage, however, tidal-currents  
183 become more effective, and salinity intrusion may extend to *ca* rkm 50 (Fox *et al.*, 1984;  
184 Chawla *et al.*, 2008; Figs 2A and 3B). Furthermore, within the MTFR, fluvial and tidal currents  
185 combine with intrabasinal wind-waves when atmospheric conditions are favourable (Fig. 4B).  
186 These short period (2.0 to 3.3 s) wind-waves possess maximum heights of 0.2 to 0.7 m with  
187 estimated near-bottom orbital velocities  $>0.2 \text{ ms}^{-1}$ , which can re-suspend up to medium sands  
188 between *ca* 1 to 4 m in depth (Peterson *et al.*, 2014). The largest wind-waves are produced by  
189 west/south-west to east/north-east oriented winds from October to April, which occur during  
190 low-river flows (Figs 3A and 4B). Conversely, smaller wind-waves are produced by  
191 north/north-west to south/south-east oriented winds from May to September that tend to develop  
192 during higher-river flows (Figs 3A and 4B). (3) The fluvially-dominated, tidally-influenced  
193 regime (FDTIR) spans *ca* rkm 56 to 235 (Fig. 3B), and at all river-stages is governed by  
194 downstream-oriented currents (Fig. 4A). At low river-stage, however, flood-tides cause fluvial-  
195 currents to experience: (i) weak reversals to *ca* rkm 109 (Clark & Snyder, 1969; Fig. 3B); and

196 (ii) cyclic velocity reduction and acceleration upstream of *ca* rkm 109. In summary, integration  
197 of all hydraulic processes operating over the LCR study reach produces a temporally averaged  
198 ‘global’ conceptual relative energy diagram (Fig. 5A), which shows that: (i) downstream-  
199 oriented currents are the first-order control on sediment transport within the MTFR, whilst  
200 upstream-oriented flood tidal-currents and intrabasinal wind-wave oscillatory-currents are  
201 second-order controls; and (ii) downstream-oriented currents dominate sediment transport within  
202 the FDTIR.

203

#### 204 **(B) Modern Lower Columbia River sediment supply**

205 The LCR mean annual sediment-load,  $Q_s$ , where  $Q_s = Q_{sand} + Q_{wash}$  (where  $Q_{sand}$  represents  
206 bedload + suspended-load particles  $>0.1$  to  $\leq 2$  mm, and  $Q_{wash}$  represents suspended-load  
207 particles  $\leq 0.1$  mm), is derived from upstream drainage basin sources and tributaries (above *ca*  
208 rkm 172), and is conveyed downvalley by large river-flows (Jay *et al.*, 1990; Sherwood *et al.*,  
209 1990; Naik & Jay, 2011), whilst very little of its modern  $Q_s$  is sourced from the continental shelf  
210 (Gelfenbaum *et al.*, 1999; Templeton & Jay, 2013). The concentration of suspended fine  
211 sediment ( $\leq 0.062$  to  $0.1$  mm;  $Q_{wash}$ ) in the LCR is strongly a function of river-stage, where peak  
212 concentrations occur during high river-flows (Haushild *et al.*, 1966; Naik & Jay, 2011;  
213 Templeton & Jay, 2013), which is also supported by LCR high-flow plume research at its mouth  
214 and along the shelf (cf. Horner-Devine *et al.*, 2009). This same relation also holds for the TM of  
215 the LCR, which displays highest suspended-sediment concentrations (SSCs) during high-river  
216 stages that diminish during low-river stages (Gelfenbaum, 1983). Moreover, Gelfenbaum (1983)  
217 estimated that the maximum thickness of TM produced slackwater neap-tide and spring-tide fine  
218 sediment layers during low-river stage would be *ca* millimetre-scale, and thus less than

219 millimetre-scale upstream of the TM where SSCs are typically lower. From *ca* rkm 0 to 35,  
220 LCR thalweg sediment,  $Q_{sand}$ , ranges from fine to medium sand (0.2 to 0.5 mm), and coarsens  
221 marginally to medium to coarse sand (0.25 to 0.75 mm) from *ca* rkm 35 to 235 (Fox *et al.*, 1984;  
222 Sherwood & Creager, 1990; Fig. 3B). Due to the sand-rich nature of the LCR, the most  
223 important component of  $Q_s$  is its  $Q_{sand}$  fraction (Templeton & Jay, 2013). However, many  
224 researchers have concluded that the  $Q_s$  of the modern LCR, and especially its  $Q_{sand}$  (after 1940),  
225 have been significantly reduced by post-dam sediment trapping, and reductions in  $Q_{Wavg}$  due to  
226 land irrigation, dam regulated discharge and climate change (Sherwood *et al.*, 1990; Gelfenbaum  
227 *et al.*, 1999; Naik & Jay, 2005; Jay & Naik, 2011; Naik & Jay, 2011; Templeton & Jay, 2013).  
228 Hindcast estimates below *ca* rkm 172 suggest that pre-1900  $Q_s$  was *ca* 20 Mt yr<sup>-1</sup> ( $Q_{sand} \approx 10$  Mt  
229 yr<sup>-1</sup>; Gelfenbaum *et al.*, 1999; Naik & Jay, 2011), but has decreased to *ca* 8 Mt yr<sup>-1</sup> ( $Q_{sand} \approx 3.2$   
230 Mt yr<sup>-1</sup>) after 1970 within the post-dam era (Naik & Jay, 2011; Fig. 5B). In comparison,  
231 analyses of the lower Columbia River Valley (LCRV; *ca* rkm 0 to 235) and continental-shelf  
232 sediment budget suggest that LCR longer-term Holocene averaged (last *ca* 10,000 yr)  $Q_s$  was 10  
233 to 20 Mt yr<sup>-1</sup>, where *ca* 75% (7.5 to 15 Mt yr<sup>-1</sup>) of this sediment was exported to the shelf, thus  
234 leaving a balance of 2.5 to 5.0 Mt yr<sup>-1</sup> to fill the LCRV to its current level (Fig. 5B; Gelfenbaum  
235 *et al.*, 1999; Baker *et al.*, 2010; Peterson *et al.*, 2013).

236 Furthermore, Templeton & Jay (2013) produced new hindcast predictions of the LCR  
237  $Q_{sand}$  fraction from *ca* 1900 to 2010, which include the  $Q_{sand}$  contributions of the Willamette  
238 and Cowlitz Rivers, to re-evaluate the balance of potential  $Q_{sand}$  supplied to the LCR below *ca*  
239 rkm 109 against that removed via dredging and sand-mining. These results suggest the LCR has  
240 experienced a net  $Q_{sand}$  deficit for >50 of the last 85 years, and since 1962 this deficit has  
241 averaged *ca* 4.6 ( $\pm 1.7$ ) Mt yr<sup>-1</sup> (Templeton & Jay, 2013). The  $Q_{sand}$  results of Sherwood *et al.*

242 (1990) and Templeton & Jay (2013) imply that since *ca* 1940 the LCR should be reacting to  
243 declining  $Q_{sand}$  via ‘natural’ channel-bed and/or barform degradation below the Bonneville Dam  
244 (cf. Williams & Wolman, 1984; Schmidt & Graf, 1990; Topping *et al.*, 2000a,b; Rubin *et al.*,  
245 2002; Grant *et al.*, 2003; Graf, 2006). However, no definitive ‘natural’ channel-bed or barform  
246 degradational observations exist, and instead: (i) the main navigation channel from *ca* rkm 5 to  
247 172 has been artificially deepened by a total of *ca* 2.4 m since 1965; and (ii) barforms, sand  
248 shoals, and floodplains, positioned between *ca* rkm 0 to 80 in peripheral bays adjacent to the  
249 navigation channel (i.e. Cathlamet Bay) have been aggrading for the last 100 to 1000 yr  
250 (Sherwood *et al.*, 1990; Peterson *et al.*, 2014; Prokocki *et al.*, 2015).

251

#### 252 **(B) Modern fluvial–tidal barform migration rates**

253 Time-sequenced aerial imagery from 1990 to 2011 (Bar BT1-P; FDTIR) and from 1990 to 2012  
254 (Bars CB1-S and CB2-W; MTFR) was utilized to measure and compare the migration rates of  
255 bars positioned within secondary less human altered channels possessing closer to natural  
256 hydraulic properties (Sherwood *et al.*, 1990) relative to the adjacent heavily dredged main  
257 navigation channel (cf. Sherwood *et al.*, 1990; Jay, 2009; Jay *et al.*, 2011; Naik & Jay, 2011;  
258 Templeton & Jay, 2013), and within differing LCR fluvial–tidal hydraulic regimes (Fig. 6A to  
259 C). By tracking the centre of each bar from 1990 to 2011, or 2012, it is shown that Bar BT1-P  
260 migrated at an average rate of *ca* 7 m yr<sup>-1</sup>, whereas Bars CB1-S and CB2-W possessed near equal  
261 average migration rates of *ca* 24 m yr<sup>-1</sup> (Fig. 6A-C). Migration patterns thus indicate that Bar  
262 BT1-P underwent primarily lateral-migration with minimal downstream translation in  
263 conjunction with vertical aggradation, whilst Bars CB1-S and CB2-W were governed by  
264 downstream translation and marginal lateral-migration (Fig. 6A to C). The differences in the

265 rates and patterns of bar migration between Bar BT1-P (FDTIR) and Bars CB1-S and CB2-W  
266 (MTFR) are due to 'local' hydraulic effects, and not 'global' hydraulic effects. For instance,  
267 from a 'global' energy perspective (Fig. 4A), Bar BT1-P (FDTIR) should experience stronger,  
268 and more frequent, downstream-oriented currents than Bars CB1-S and CB2-W (MTFR). Thus,  
269 the 'global' expectation is that Bar BT1-P should display faster downstream migration rates than  
270 Bars CB1-S and CB2-W, but instead the opposite is true. This is because 'locally' Bar BT1-P  
271 formed in a secondary channel arm of the LCR that is cut-off from LCR discharge, which is  
272 mainly confined to the adjacent main navigation channel (Fig. 6A). Conversely, Bars CB1-S and  
273 CB2-W formed within Prairie/Woody Island Channel network, Cathlamet Bay (i.e. secondary  
274 channel arm to adjacent main navigation channel; Fig. 6B and C), which 'locally' still receives a  
275 significant portion of LCR discharge and downstream-oriented current energy (cf. Sandbach *et*  
276 *al.* 2018). Therefore, even though Bars CB1-S and CB2-W exist in a lower 'global'  
277 downstream-oriented current regime when compared to Bar BT1-P (Fig. 4A), the 'local'  
278 frequency and magnitude of downstream-oriented current energy remains greater in the  
279 Prairie/Woody Island Channel network (MTFR) *versus* the south arm secondary channel of the  
280 FDTIR where Bar BT1-P formed.

281         Herein, the sedimentological details and interpretations of these three migrating FTT  
282 mid-channel bars of the LCR are presented. The first barform investigated (Bar BT1-P; rkm 80;  
283 FDTIR) formed within freshwater upstream of both the zone of TM development and salinity  
284 intrusion (Fig. 2A), where *ca* 3.5 km of GPR data (13 transects) and three vibracores were  
285 collected (Fig. 2B). Next, two barforms (Bar CB1-S and CB2-W) were analysed within the  
286 upper-MTFR, which are located upstream of the zone of TM development, but near the  
287 maximum extent of present low-river stage salinity intrusion, within Prairie Channel, Cathlamet

288 Bay (Fig. 2C and D). At Bar CB1-S (*ca* rkm 42), *ca* 3.9 km of GPR data (12 surveys) and three  
289 vibracores were extracted, whereas *ca* 3.8 km of GPR data (17 surveys) and three vibracores  
290 were collected at Bar CB2-W (Fig. 2A). This data represents the first high-resolution  
291 geophysical and sediment core observations of modern FTT barforms that formed within a multi-  
292 channelled sand-bed, large-river ( $Q_{Wavg}$  *ca* 7000 m<sup>3</sup> s<sup>-1</sup>, and  $Q_{Wpeak} \geq 15,000$  m<sup>3</sup> s<sup>-1</sup>), and that  
293 were potentially influenced by river-currents, and/or long period (tidal) and short period (wind-  
294 wave) oscillatory-currents.

295

## 296 (A) METHODS OF ANALYSIS

### 297 (B) Ground penetrating radar surveying and post-processing

298 Common-offset GPR transects (42 in total; *ca* 11.2 km) were collected via a Sensors & Software  
299 pulse-EKKO 100 smartcart system (Sensors & Software Inc., Mississauga, Ontario, Canada)  
300 upstream of the region of saltwater saturation. Radar velocity through the freshwater-saturated  
301 sediment was determined from common mid-point surveys (CMPs) using normal move-out  
302 corrections. Two-way travel time was then converted to depth using a constant velocity of 0.054  
303 m ns<sup>-1</sup> ( $\pm 0.004$ ), where the maximum depth of imaging was *ca* 10 m. Post-processing of survey-  
304 lines was completed in Seismic Unix software, which included: (i) the application of a zero-  
305 phase, sine-tapered bandpass filter with polygon frequency values of 10, 50, 250 and 600 MHz;  
306 (ii) time-based gaining of the data to reduce loss of reflection amplitude with depth; and (iii)  
307 Stolt-migration based on a single subsurface velocity to reduce refraction hyperbolae. All GPR-  
308 profiles were then interpreted by classifying the most prominently repeating reflector geometries  
309 into distinct radar facies (see Best *et al.*, 2003; Sambrook Smith *et al.*, 2006, 2009; Mumpy *et al.*,  
310 2007; Ashworth *et al.*, 2011; Parker *et al.*, 2013; Reesink *et al.*, 2014). Following the approach

311 of Sambrook Smith *et al.* (2006, 2009), the areal occurrence (%) of each radar facies was  
312 computed for all GPR-profiles collected to examine the spatial distribution of facies within each  
313 bar. Next, the vertical occurrence (%) of facies within each bar was analysed by dividing each  
314 GPR-profile into regular intervals (1 m thick), as measured upward from the barform base. The  
315 proportion of facies within each vertical interval was then determined and summed, thus  
316 enabling the quantification of vertical facies distributions.

317

### 318 **(B) Vibracore collection and analysis**

319 Vibracores ( $\leq 5$  m depth) were extracted using a *ca* 0.076 m diameter aluminium irrigation pipe  
320 vibrated to depth by a portable vibracore rig. At each of the three barforms investigated (Fig. 2A  
321 to D), a single vibracore was taken from the head, mid-bar and bartail, to capture potential  
322 sedimentological variation parallel to flow-direction (total of three cores per bar). After  
323 extraction, all cores were cut in half lengthways, where one half was set in epoxy resin to  
324 preserve sedimentary structures, whilst the other half was used for grain-size sampling. Grain-  
325 size samples were collected every *ca* 0.2 m from the base of each core to its top, and in unique  
326 horizons such as silt drapes and coarse-grained interbeds. All samples were analysed via laser-  
327 diffraction size analysis (LDSA) using a Malvern Mastersizer 2000 (Malvern Instruments  
328 Limited, Malvern, UK) to acquire: (i) their relative percentage of clay ( $<0.0039$  mm), silt  
329 ( $>0.0039$  to  $<0.063$  mm) and sand ( $>0.063$  to  $<2$  mm) particles; and (ii) grain-size distributions.  
330 Additionally, the Folk & Ward (1957) sorting index was computed for each sample. The  $D_{50}$   
331 grain size and sediment sorting results of individual cores were then plotted against descriptive  
332 sedimentary logs to identify fining-upward and coarsening upward and sediment sorting trends in  
333 relation to the preserved depositional fabrics. These core results were then applied to the

334 corresponding GPR-profiles in order to ground-truth the sedimentological interpretation of radar  
335 facies.

336

## 337 (A) RESULTS

### 338 (B) Sedimentology of radar facies

339 The general descriptions, spatial-scales, and examples, of the four radar facies identified in GPR-  
340 transects are presented in Table 2. However, the following will only explore the detailed  
341 sedimentological observations and variations for the three primary radar facies (facies 1 to 3;  
342 Table 2) preserved within individual, and between FTT barforms, via specific GPR-profile  
343 examples and associated vibracore sedimentary logs. Radar facies 4 is excluded from analysis  
344 beyond that provided in Table 2, because no sedimentological evidence was observed in the  
345 vibracores obtained, and its representation within barforms is insignificant ( $\leq 0.01\%$  in  
346 occurrence) relative to facies 1 to 3. Lastly, Table 3 presents the key to sedimentary logs, and  
347 defines pertinent tidal-elevation and wind-elevation markers displayed on GPR-profiles and core  
348 logs.

349

### 350 (C) Radar facies 1a (Bar BT1-P; FDTIR)

351 **Description:** Facies 1a consists of stacked, continuous, low-angle ( $< 5^\circ$ ) parallel reflectors  
352 composed of clean cross-laminated moderately to well-sorted fine to medium sands with  
353 interbeds of thin ( $< 0.05$  m thick) concentrated horizons of organic detritus, sporadic inclusions of  
354 organic debris, and a homogenous *ca* 0.4 m thick interbed of silt-rich very poorly-sorted very-  
355 fine sand bounded above and below by clean moderately-well to well-sorted fine to medium  
356 sands (Fig. 7A).

357 **Interpretation:** In the FDTIR, facies 1a represents low-angle dipping ( $<5^\circ$ ) upper-subtidal to  
358 intertidal bartail deposits (profile BT1-PY3, Fig. 8) formed by the aggradation of current-ripples  
359 to small-dunes that can be interbedded with up to *ca* 0.4 m thick cross-laminated silty very-fine  
360 sand horizons. Fine-grained interbeds form via suspended-sediment fallout, and subsequent  
361 reworking, into current-ripples within the low-velocity bartail recirculation-cell produced by  
362 flow-separation around bars during a single, or multiple, high-river stage event(s) (cf. Leeder &  
363 Bridges, 1975; Nanson & Page, 1983; Smith *et al.*, 2009, 2011; Moreton & Carter, 2015).

364

365 **(C) Radar facies 1b (Bar CB1-S; upper-MTFR)**

366 **Description:** Facies 1b is imaged as stacked, continuous, low-angle ( $<5^\circ$ ) parallel reflectors, and  
367 consists of clean cross-laminated moderately-well to well-sorted fine to medium sands with  
368 sporadic to abundant ( $<0.08$  m thick) planar-laminated macroscopic organic horizons with, or  
369 without, pumice gravel. Facies 1b fines-upward from its base (i.e. becomes dirtier) before  
370 coarsening-upward and becoming better sorted towards its top (Fig. 9A to C). However, facies  
371 1b does vary across Bar CB1-S (barhead to bartail) with respect to the frequency, thickness, and  
372 fabric, of silt to very-fine sand intervals, which can be (Fig. 9A to C): (i) a *ca* 1 m thick  
373 heterogeneous bed with interbedded  $<0.08$  m thick organic layers and  $<0.1$  m thick horizons of  
374 cross-laminated fine sands (barhead); (ii) infrequent thin ( $\leq 0.05$  m thick) silt drapes (mid-bar); or  
375 (iii) completely absent (bartail). Facies 1b typically overlies facies 2 or 3, but may interbed with  
376 facies 3 near bar-tops (*ca* 0 to 3 m depth; Fig. 10).

377 **Interpretation:** Facies 1b is interpreted as the reworking of bartop upper-subtidal to intertidal  
378 three-dimensional trough cross-stratified to high-angle ( $>5^\circ$ ) cross-bedded dune to unit-bar scale  
379 deposits, generated by the combined-influence of intrabasinal wind-waves and tidally-produced

380 cyclic shallow water flooding and drainage currents (cf. Prokocki *et al.*, 2015) that form low-  
381 angle dipping ( $<5^\circ$ ) longitudinal and lateral bar accretion packages (Fig. 10). Similar low-angle  
382 accretion-units in subaqueous sandbanks of the Marennes-Oleron Bay, France, have been  
383 observed, and are likewise interpreted to be the product of oceanic wave-tidal combined-flows  
384 (see figs 9 to 11 of Chaumillion *et al.*, 2008). Furthermore, when facies 1b displays abundant  
385 silt/very-fine sand drapes ( $<0.05$  m thick), or silty-sand horizons (0.1 to  $>0.4$  m thick), this  
386 represents: (i) high-river discharge  $Q_{wash}$  sediment-fallout within recirculation-cells produced by  
387 flow-separation around Bar CB1-S, or flow deceleration of downstream-oriented currents caused  
388 by flow divergence at swatchway entrances (i.e. barhead of Bar CB1-S); and/or (ii) low-river  
389 stage re-entrainment, and redistribution, of high river-stage and/or slackwater deposited  $Q_{wash}$   
390 (potentially from bartail towards barhead) via intrabasinal wind-waves working in conjunction  
391 with flood-tidal currents.

392

393 **(C) Radar facies 1c (Bar CB2-W; upper-MTFR)**

394 **Description:** Facies 1c is also depicted as stacked, continuous, low-angle ( $<5^\circ$ ) parallel  
395 reflectors, but unlike facies 1a and 1b, it exists typically from bartail to barhead as bioturbated  
396 fine to medium sands with sporadically preserved plant debris or pumice gravel with (Fig. 11A  
397 to C): (i) intensely bioturbated, or churned, horizons ( $>0.1$  to  $<1.5$  m thick) of silt to fine-sand  
398 (Fig. 11B and C); or (ii) abundant silt drapes that are  $<0.05$  m thick. However, low-angle planar  
399 to cross-laminated sets are present in horizons with minimal bioturbation. Similar to facies 1b,  
400 facies 1c tends to fine-upward from its base, and then coarsens and becomes better sorted upward  
401 near its top (Fig. 11B and C), but only displays a coarsening-upward and sorting-upward trend  
402 from its base to top in bartail alluvium (Fig. 11A). Facies 1c typically overlies facies 2 or 3, and

403 like facies 1b tends to be interbedded with facies 3 near bar-tops (ca 0 to 3 m depth; Line CB2-  
404 WX6; Fig. 12).

405 **Interpretation:** Similar to facies 1b, facies 1c also represents the reworking of bartop upper-  
406 subtidal to intertidal 3D trough cross-stratified to high-angle ( $>5^\circ$ ) cross-bedded dune to unit-bar  
407 scale deposits into low-angle dipping ( $<5^\circ$ ) longitudinal and lateral bar accretion packages (Fig.  
408 12). The abundant silt to very-fine sand drapes and intervals are interpreted as  $Q_{wash}$  sediment-  
409 fallout within recirculation-cells produced by flow-separation around Bar CB2-W during high-  
410 river discharge, and/or low-river stage redistribution of high-river stage and/or slackwater  
411 produced silts to very-fine sands via intrabasinal wind-waves in association with tidal-currents.  
412 However, since facies 1c is much dirtier and bioturbated relative to facies 1b, it is thought that  
413 the rates, and strength, of wind-wave reworking of alluvium are weaker during the creation of  
414 facies 1c.

415

416 **(C) Radar facies 2a: (Bar BT1-P; FDTIR)**

417 **Description:** Facies 2a is imaged as high-angle ( $>6^\circ < 20^\circ$ ) inclined reflectors composed of  
418 planar to cross-laminated bedded moderately-well to well-sorted fine to medium sands with  
419 sporadic organic debris, a few thin ( $<0.08$  m thick) interbeds of concentrated organic detritus,  
420 and several  $<0.05$  m thick silty very-fine sand drapes (Fig. 7B). This facies also shows a  
421 marginal fining-upward trend from well-sorted basal medium sands to dirtier, moderately well-  
422 sorted, fine sands, whose silt rich intervals are poorly-sorted (Fig. 7B).

423 **Interpretation:** Facies 2a represents high-angle dipping subtidal to intertidal bar-margin lateral-  
424 accretion sets (Line BT1-PX5; Fig 8), where fine-grained interbeds are the product of non-cyclic,  
425 or sporadic, suspension fall-out of  $Q_{wash}$  during high-fluvial discharge intervals within low-

426 velocity sidebar recirculation-cells that are created as seaward-directed main flow detaches  
427 around barheads.

428

429 **(C) Radar facies 2b: (Bar CB2-W; MTFR)**

430 **Description:** Facies 2b consists of high-angle inclined reflectors composed of silt-rich  
431 moderately to very-poorly sorted very-fine to fine sands that are intensely bioturbated, but cross-  
432 laminae sets are present where bioturbation is less intense (Fig. 11A).

433 **Interpretation:** This facies is interpreted as subtidal avalanche faces of prograding bartail  
434 accretion-sets (Fig. 12), where silt drapes to bioturbated silty-sand horizons are the product of: (i)  
435 non-cyclic capture of high-river stage  $Q_{wash}$  within low-velocity bartail recirculation-cells; (ii)  
436 more cyclic deposition of high-river stage  $Q_{wash}$  during flood-tides, and tidal slackwater, when  
437 the velocity of downstream-oriented currents is reduced; (iii) low-river stage re-entrainment of  
438  $Q_{wash}$  via wind-waves and tidal-currents that is more cyclically redeposited during tidal  
439 slackwaters, and/or redeposited as suspended-sediment fallout when wave-energy diminishes; or  
440 (iv) a combination of (i), (ii) and (iii).

441

442 **(C) Radar facies 3 (FDTIR and MTFR)**

443 **Description:** Throughout all FTT regimes, facies 3 consists of stacked-sets of laterally-  
444 discontinuous undular (concave-up or concave-down) to chaotic reflectors, which are composed  
445 of clean moderately-well to well-sorted cross-bedded medium sands with sporadic interbeds  
446 (<0.08 m thick) of concentrated organic debris and gravel-sized pumice stones (Fig. 7A to C).  
447 Facies 3 occurs as barhead to bartail alluvium that fines-upward from base to top, but may  
448 possess second-order decimetre-scale fining and coarsening-upward sequences (Fig. 7A).

449 Within the FDTIR, facies 3 is deposited at subtidal to intertidal elevations (Fig. 8), whilst it is  
450 more commonly preserved at subtidal depths within the MTFR (Figs 10 and 12).

451 **Interpretation:** Facies 3 represents vertically-stacked 3D dune to unit-bar trough-cross and  
452 cross-bedded deposits within longitudinal and lateral-accretion packages, which are commonly  
453 found in river braid-bars (cf. Bridge, 1993; Bridge *et al.*, 1998; Bridge, 2006). The largest  
454 trough-shaped reflectors are found at greater depths (*ca* 6 to 10 m), whilst progressively  
455 becoming smaller-scale towards bartops (Fig. 8). This vertical gradient in reflectors corresponds  
456 to a decrease in flow depth towards bartops, which forces a reduction in the height and  
457 wavelength of dunes and unit-bars (Yalin, 1964; Allen, 1978). Parallel reflectors in this facies  
458 are thus bounding surfaces between either (Fig. 8): (i) dune-scale cross-sets; (ii) unit-bar  
459 accretion-sets; or (iii) bar-scale accretion-sets.

460

#### 461 **(B) Patterns of bar migration and occurrence of radar facies**

#### 462 **(C) Bar BT1-P: FDTIR**

463 From 1990 to 2011, Bar BT1-P underwent primarily vertical aggradation, but also experienced  
464 relatively slow (*ca* 7 m yr<sup>-1</sup>; Fig. 6A) southward-directed lateral-accretion, and marginal  
465 elongation via bartail-extension and barhead-accretion (see Supplemental Information). Within  
466 this context, the architecture of Bar BT1-P is dominated by facies 3 ( $\geq 70\%$  areal occurrence in  
467 all GPR-transects; Fig. 13A). In the vertical, the occurrence of facies 3 is  $>80\%$  from its base to  
468 bar-top (10 to 0 m depth; Fig. 13B), but can be  $>95\%$ . However, facies 1a and 2a do exist in  
469 relatively low-occurrences between 0 to 6 m depth ( $\leq 11\%$ ; Fig. 13B), but are restricted to  
470 southern bar-margin lateral-accretion and bartail-extension (see lateral-lines PX4-PX9, and  
471 longitudinal-lines PY1, PY3 and PY4; Fig. 13A).

472 (C) Bar CB1-S: MTFR

473 Between 1990 and 2012, this bar experienced relatively high-rates of downstream-translation (*ca*  
474 24 m yr<sup>-1</sup>; Fig. 6B) that transformed its morphology from elongated to more arcuate, which  
475 promoted development of bartail-limbs (see Supplemental Information). Relative to Bar BT1-P,  
476 Bar CB1-S possesses a different morphology (arcuate *versus* elongated), and developed within a  
477 differing hydraulic context punctuated by dominant seaward-oriented currents, stronger  
478 upstream-oriented flood-tidal currents, and intrabasinal wind-waves. Given these differences,  
479 the resulting architecture of Bar CB1-S varies from that of Bar BT1-P in several ways. First, in  
480 Bar CB1-S profiles, the overall occurrence of facies 3 reduces by *ca* 30 to 60% to ≤45% within  
481 longitudinal-transects (SY1 to SY4), and reduces by *ca* 10 to 60% to ≤60% in lateral-profiles  
482 (SX1 to SX8; compare Figs 13A and 14A). Secondly, facies 1 transforms into facies 1b, and  
483 increases in occurrence by *ca* 40 to 85% to ≥55% in longitudinal-profiles, whilst increasing to  
484 between 10 to 85% in lateral-lines (Fig. 14A). Thirdly, at Bar CB1-S, facies 1b displays a  
485 continual increase in occurrence from its base to bartop, where it is ≤7% from 5 to 7 m depth,  
486 whilst drastically increasing to *ca* 34 to 55% from 3 to 5 m depth, which is within the projected  
487 depth window of intrabasinal wind-wave influence at MLLW (MaxW2; Fig. 14B). Facies 1b  
488 then further increases in abundance to *ca* 80 to 90% within the depth window of intrabasinal  
489 wind-wave activity at MHHW (MaxW1; 0 to 3 m depth) near its top (Fig. 14B).  
490 Simultaneously, from its base to bartop, facies 3 decreases in occurrence from *ca* 60 to 96% from  
491 4 to 7 m depth to <30% from 0 to 4 m depth through MaxW2 and MaxW1 (Fig. 14B).  
492 Furthermore, facies 2a also exists in relatively low-occurrence (<2%) from 4 to 7 m depth before  
493 notably increasing to *ca* 13 to 17% near its bartop (*ca* 2 to 4 m depth; Fig. 14B). These facies

494 trends do not exist at Bar BT1-P, which is dominated from base to bartop by the vertical-stacking  
495 of facies 3.

496

497 **(C) Bar CB2-W: MTFR**

498 From 1990 to 2012, Bar CB2-W (positioned *ca* 2 km south-west of Bar CB1-S within  
499 Prairie/Woody Island Channel) underwent (Fig. 6C, and Supplemental Information): (i)  
500 downstream translation equal to *ca* 24 m yr<sup>-1</sup>; (ii) volumetric growth in the form of lateral-  
501 expansion; and (iii) development of bartail-limbs. Since Bars CB1-S and CB2-W are located  
502 within the same channel and FTT regime, share a similar arcuate morphology, and experienced  
503 analogous migration rates and patterns, the expectation is that they will possess nearly identical  
504 facies occurrences and stacking patterns. In general, the architecture of these two bars are more  
505 closely related to one another than Bar BT1-P, but there are several notable differences. First, at  
506 Bar CB2-W, facies 1 transforms into facies 1c and facies 2 becomes facies 2b. Secondly, in  
507 general, the longitudinal-profiles of Bar CB2-W also mainly comprise facies 1 ( $\geq 45\%$ ; form of  
508 facies 1c) and facies 3 (0 to 55%; Fig. 15A), but they possess a *ca* 2 to 15% higher occurrence of  
509 facies 2 (form of faces 2b) relative to facies 2a at Bar CB1-S (see Figs 14A and 15A). Thirdly,  
510 the barhead to bartail lateral-lines (WX1 to WX11) of Bar CB2-W have a higher (*ca* 40% on  
511 average) abundance of facies 3, and an average lower occurrence (*ca* 25%) of facies 1 in the  
512 form of facies 1c.

513         Furthermore, in the vertical direction at Bar CB2-W, facies 1c continually increases in  
514 occurrence from its base to bartop, as also observed in facies 1b at Bar CB1-S, but the pattern of  
515 this increase differs. Within Bar CB2-W, the occurrence of facies 1c spans *ca* 6 to 18% between  
516 3 to 6 m depth (base of MaxW2), which then increases rapidly at the base of MaxW1 to *ca* 45%

517 at 2 to 3 m depth, and then continues to increase towards the top of MaxW1 from *ca* 60% (1 to 2  
518 m depth) to *ca* 70% between 0 to 1 m depth (Fig. 15B). Comparatively, at Bar CB1-S, facies 1b  
519 has a much higher occurrence ( $\geq 30$  to 82%) throughout the 3 to 5 m depth interval (i.e. within  
520 MaxW2), and does not decline below *ca* 10% until below MaxW2 at 5 to 6 m depth (Fig. 14B).  
521 Secondly, and resembling the trend at Bar CB1-S, the occurrence of facies 3 here also decreases  
522 from base to bartop, but not to the same degree. At Bar CB2-W, the occurrence of facies 3 is  
523  $\geq 70\%$  between 3 to 7 m depth (i.e. from within MaxW2 to below MaxW2) before reducing  
524 through MaxW1 to *ca* 45% (2 to 3 m depth), and then to *ca* 25% from 0 to 2 m depth (Fig. 15B).  
525 Relative to Bar CB1-S, however, the average preservation of facies 3 is much greater (*ca* +25%)  
526 from 0 to 5 m depth through the MaxW2 and MaxW1 wind-wave windows. The final  
527 divergence in facies occurrence with depth between Bars CB1-S and CB2-W appears within the  
528 depth interval spanning 0 to 2 m, where at Bar CB2-W the proportion of facies 2b ranges from  
529 *ca* 8 to 15%, whilst at Bar CB1-S any style of facies 2 is absent (see Figs 14B and 15B).

530

## 531 (A) DISCUSSION

### 532 (B) Linking fluvial–tidal transition hydraulics to barform architecture and inclined 533 heterolithic stratification

#### 534 (C) Large-river FDTIR mid-channel bars

535 Although Bar BT1-P (FDTIR) experiences cyclic bidirectional-currents and slackwater intervals,  
536 its architecture is nearly identical to that of linear, or elongated, fluvial braid-bars experiencing  
537 more vertical-aggradation relative to lateral and/or longitudinal-accretion (cf. Sambrook Smith *et al.*,  
538 2006, 2009; Mumpy *et al.*, 2007; Ashworth *et al.*, 2011; Parker *et al.*, 2013; Reesink *et al.*,  
539 2014). Thus, downstream-oriented currents, especially river-flood events (Dalrymple *et al.*,

540 2015), govern the bed to bar-scale sedimentology of LCR braid-bars throughout its FDTIR,  
541 whilst flood-tidal currents, and slackwater periods (four daily), seem to exert little influence.  
542 This finding is supported by: (i) fluvial dominance throughout the FDTIR of the LCR (Fig. 4A);  
543 and (ii) the numerical simulations of van de Lageweg & Feldman (2018) who found that the  
544 landward-most braid-bars within micro-tidal to meso-tidal range FTTs tend to have a  
545 sedimentological architecture dominated by seaward-oriented currents. Therefore, with respect  
546 to longer-term preservation, this suggests that *ca* 76% (*ca* rkm 56 to 235; FDTIR) of the LCR  
547 basal to bar-top braid-bar successions within its FTT will be indistinguishable from upstream  
548 fully-fluvial braid-bars.

549         Moreover, this finding also suggests that FDTIR braid-bar bartail and bar-margin  
550 accretion-sets with sporadic silty very-fine sand horizons (>0.2 m thick) and thin (<0.05 m thick)  
551 silty very-fine sand drapes, are unlikely to be tidally-produced IHS packages as commonly  
552 interpreted (cf. Smith, 1987; Sisulak & Dashtgard, 2012; Johnson & Dashtgard, 2014; Dalrymple  
553 *et al.*, 2015). Instead, they represent fluvially derived decimetre-scale low-angle (<5°) non-  
554 cyclic IHS of bartail accretion-sets, and high-angle (>5° ≤20°) sub-decimetre scale bar-margin  
555 non-cyclic IHS within lateral-accretion units (Fig. 16A). These IHS packages are likely  
556 deposited during high-river stage(s) within low-velocity bartail and side-bar flow recirculation-  
557 cells when LCR river-derived  $Q_{wash}$  concentrations are highest (cf. Haushild *et al.* 1966; Naik &  
558 Jay, 2011; Templeton & Jay, 2013). Furthermore, these are the same hydraulic-sedimentation  
559 processes that produce fluvial IHS in bartail and lateral-accretion sets of modern sand-bed,  
560 large-river braid-bars (Bristow, 1993; Best *et al.*, 2003; Reesink *et al.*, 2014), modern and  
561 ancient counter point-bar accretion-sets (Smith *et al.*, 2009, 2011; Durkin *et al.*, 2015), and

562 downstream most point-bar lateral-accretion successions (Thomas *et al.*, 1987; Hubbard *et al.*,  
563 2011; Durkin *et al.*, 2015; Moreton & Carter, 2015).

564

565 **(C) Large-river MTFR mid-channel bars**

566 Bars CB1-S and CB2-W display relatively high rates of downstream-translation, arcuate  
567 morphologies, and associated bartail-limb construction, which are typical attributes of migrating  
568 fluvial and/or fluvial-tidal braid-bars (cf. Ashworth, 1996; Best *et al.*, 2003; Reesink *et al.*, 2014;  
569 Leuven *et al.*, 2016). Thus, similar to FDTIR braid-bars of the LCR, these patterns of  
570 morphology and migration suggest that seaward-directed currents, especially high-river flows,  
571 govern their bed to bar-scale sedimentology, which is not surprising since the mesotidal LCR is  
572 fluvially, or ebb-tidal, dominant. Given this context, the stratal architectures of Bars CB1-S and  
573 CB2-W should be similar to one another, as well as FDTIR braid-bars, and should also be  
574 comparable to other sand-bed, large-river braid-bars undergoing downstream-translation (i.e. Río  
575 Paraná, Argentina; see Sambrook Smith *et al.*, 2009; Reesink *et al.*, 2014). However, Bars CB1-  
576 S and CB2-W do not possess a similar architecture to FDTIR bars, nor are they identical to one  
577 another (see Figs 13, 14 and 15), and their architecture is incongruous with translating Río  
578 Paraná bars.

579 For instance, bars of the Río Paraná tend to have stratal architectures dominated by  
580 relatively clean longitudinal and lateral-accretion packages composed of (Sambrook Smith *et al.*,  
581 2009; Reesink *et al.*, 2014): (i) mid-bar to bar-top high-angle ( $>20^\circ$  to angle of repose) to  
582 medium-angle ( $>6^\circ <20^\circ$ ) cross-strata associated with the migration of small to large-dunes,  
583 unit-bars, or bar-margin accretion (analogous to facies 2a of this study); and (ii) basal vertically-  
584 stacked large to small-scale trough cross-strata associated with migrating 3D dunes to unit-bars

585 (analogous to facies 3 of this study). Comparatively, the basal strata of Bars CB1-S and CB2-W  
586 are similar to the Río Paraná and FDTIR bars of the LCR, except their bar-tops (*ca* 0 to 4 m  
587 depth) display minimal preservation of high to medium-angle cross-strata (facies 2a), and/or  
588 vertically-stacked trough-cross strata (facies 3), and instead consist of stacked-successions of  
589 low-angle ( $<5^\circ$ ) accretion, or facies 1b and 1c. Given that the stratal architecture of Bars CB1-S  
590 and CB2-W differ from one another, and are dissimilar to translating Río Paraná bars and FDTIR  
591 bars of the LCR, this implies that their overall sedimentology, especially bar-tops, is not solely  
592 the product of downstream-oriented currents, but must also reflect a secondary hydraulic-  
593 sedimentation response. At first glance, this finding supports the general view that mesotidal  
594 MTFR braid-bars of any FTT, regardless of fluvial-energy input (i.e. fluvial-discharge), should  
595 display a more complex bed to bar-scale architecture in comparison to up-dip FDTIR and fluvial  
596 braid-bars due to increased bidirectional tidal-current energy (especially flood-tidal currents) and  
597 associated slackwater intervals (Dalrymple *et al.*, 2015; van de Lageweg & Feldman, 2018).  
598 However, the more complex bar-top architectural styles observed within MTFR Bars CB1-S and  
599 CB2-W are not simply the product of increased bidirectional tidal-current energy, and associated  
600 slackwater intervals. Instead, these differences are interpreted herein to be the product of  
601 combined-flows consisting of a wind-wave oscillatory-current component and a bidirectional  
602 tidal-current component. One of the effects of this flow-field is reflected in the different  
603 locations, depositional fabrics, and styles, of bar-top IHS preserved within upper-MTFR bars  
604 (Fig. 16B and C).

605           Similar to Bar BT1-P (FDTIR), the majority of fine-grained sediment ( $<0.125$  mm)  
606 preserved in the bar-top deposits of Bars CB1-S and CB2-W most likely originate from high-  
607 river stage events when  $Q_{wash}$  concentrations are highest, whilst very little comes from low-river

608 stage slackwater intervals (cf. Gelfenbaum, 1983). Thus, IHS within these bars is expected to be  
609 concentrated within bartail and bar-margin accretion for the same reasoning applied to the IHS of  
610 Bar BT1-P. At Bar CB1-S, however, bartail-accretion is devoid of IHS, whilst low-angle ( $<5^\circ$ )  
611 sub-decimetre scale cyclic IHS occurs in mid-bar accretion, and low-angle combined sub-  
612 decimetre to decimetre-scale cyclic IHS exists within barhead deposits (Fig. 16B). In  
613 comparison, bartail accretion at Bar CB2-W displays bioturbated sub-decimetre to decimetre-  
614 scale high-angle ( $>5^\circ$  to  $\leq 20^\circ$ ) cyclic IHS that is bounded above by bioturbated sub-decimetre  
615 scale low-angle ( $<5^\circ$ ) cyclic IHS, whereas both mid-bar and barhead accretion-units possess  
616 bioturbated sub-decimetre scale low-angle cyclic IHS (Fig. 16C). Relative to large-river, fully-  
617 fluvial and FDTIR braid-bars, these MTFR bar-top variations in the character, depositional fabric  
618 and/or locations of IHS, represent a new category of IHS. This style of IHS is interpreted to be  
619 the result of the re-entrainment, and redistribution, of fines deposited during high-river stage(s)  
620 by low-river stage combined-flows possessing differing magnitudes of a short period wind-wave  
621 oscillatory-current component and a long period bidirectional tidal-current component (with  
622 associated slackwater intervals) that will vary in strength over neap–spring tidal cycles (Fig. 16B  
623 and C). This type of hydraulic-sedimentation response has not been documented before as a  
624 potential agent of IHS production within fluvial-tidal barforms (e.g. Smith, 1987; Thomas *et al.*,  
625 1987; Sisulak & Dashtgard, 2012; Dalrymple *et al.*, 2015; Jablonski & Dalrymple, 2016).

626         Nevertheless, the effects of varying degrees of wind-wave oscillatory-current strength  
627 creates distinctive patterns of bar-top upper-MTFR IHS. Stronger and more frequent wind-wave  
628 activity causes the absence of IHS in bartail-accretion due to the re-suspension and removal of  
629 finer sediment from accretion-units that is then re-deposited in mid-bar and barhead  
630 recirculation-cells generated by flow-separation around bars during flood-tidal flows, and/or

631 during slackwater intervals (Fig. 16B), or this re-suspended fine sediment is carried downstream  
632 away from the bartail by ebb-currents. Conversely, weaker, and less frequent, wind-wave  
633 activity allows for the development of bioturbated, and more abundant, IHS preserved within  
634 bartail to barhead accretion-sets, which experience overall lower rates of re-suspension, and thus  
635 redistribution of fines by tidal-currents (Fig. 16C). Lastly, when considering longer-term  
636 preservation across the FTT of the LCR, these findings suggest that *ca* 82% (*ca* rkm 42 to 235;  
637 upper-MTFR to FDTIR) of basal braid-bar deposits are likely indistinguishable from up-dip  
638 fully-fluvial braid-bars, whilst, if preserved, upper-MTFR bar-top strata potentially mark the  
639 facies transition from fully-fluvial to wave-tidally dominated strata.

640

641 *(C) Fluvial-tidal inclined heterolithic stratification preservation: mid-channel bars versus point-*  
642 *bars*

643 The IHS preserved within the upper-MTFR to FDTIR bars of the LCR diverge from the IHS  
644 model for fluvial-tidal point-bars (Fig. 1) in several key ways. First, fluvial to fluvial-tidal point-  
645 bar IHS tends to have dip-angles  $\geq 5^\circ$  to  $\leq 35^\circ$  (more commonly *ca* 5 to 15°) that do not vary  
646 spatially across a point-bar since their dip-angles are set by the transverse point-bar slope  
647 (Thomas *et al.*, 1987; Smith *et al.*, 2009; Durkin *et al.*, 2015; Moreton & Carter, 2015; Jablonski  
648 & Dalrymple, 2016). Furthermore, their fine-grained components of IHS are nearly always  
649 interpreted to reflect the hydraulic-sedimentation response of tidal processes (for example, tidal  
650 slackwater or turbidity-maximum enhanced deposition of fines) in conjunction with increased  
651 salinity-levels and brackish water ichnofacies (cf. Sisulak & Dashtgard, 2012; Johnson &  
652 Dashtgard, 2014; Dalrymple *et al.*, 2015). In contrast, LCR bar-top IHS of upper-MTFR to  
653 FDTIR braid-bars typically possess lower dip-angles ( $< 5^\circ$ ) that are spatially more variable (can

654 be  $>5^\circ$  to  $\leq 20^\circ$ ; Fig. 16A to C), and formed in primarily freshwater conditions upstream of the  
655 turbidity-maximum, and typically lack bioturbation (with the exception of Bar CB2-W).  
656 Secondly, FDTIR bar-top IHS is produced solely by river hydraulic-sedimentation processes  
657 within a known tidally-influenced regime, whilst upper-MTFR bar-top IHS largely reflects  
658 varying degrees of intrabasinal wind-wave oscillatory-current strength, and/or frequency, with  
659 the secondary influence of tidal-currents, and associated slackwater intervals. Thirdly, any  
660 increase in the relative density and thickness of fine-grained interbeds within LCR bar-top IHS  
661 (i.e. overall increase in mud/silt to sand ratios of bars) from the FDTIR to upper-MTFR (as  
662 would be predicted by the fluvial-tidal point-bar model), depends upon the position of individual  
663 bars relative to the maximum intrabasinal wind-wave energy corridor. For example, bars located  
664 near the centre of the wind-wave energy corridor (Bar CB1-S) will be cleaner relative to much  
665 dirtier laterally-adjacent bars (Bar CB2-W) positioned closer to basin-bounding floodplain/tidal-  
666 flat environments that are laterally separated from the strongest, and most frequent, wind-wave  
667 energy pathway (cf. van de Lageweg *et al.*, 2018; Fig. 16B and C).

668

669 **(C) Does bar-top coarsening-upward occur in fluvio-tidal mid-channel bars?**

670 A number of studies (Mutti *et al.*, 1985; Clark & Reinson, 1990; Shanmugam *et al.*,  
671 2000; Feldman *et al.*, 2008; Feldman & Demko, 2015) have suggested that tidal-bars display an  
672 overall upward-coarsening sequence towards their tops. One possibility is that this is the result  
673 of differing coarse-grained sediment transport pathways during flood and ebb-tidal flows on, and  
674 around, barforms (cf. Ghinassi *et al.*, 2018). However, the present data illustrate that the  
675 sedimentology of mid-bar to bar-top (*ca* 0 to 4 m depth) alluvium of FDTIR braid-bars (Bar  
676 BT1-P) displays an overall fining-upward sequence (Fig. 17A), whilst remaining moderately

677 well to well-sorted except in a few horizons of non-cyclic IHS. Thus, sandy FDTIR bars of the  
678 LCR contradict the upward-coarsening observations of interpreted tidal-bars (cf. Mutti *et al.*,  
679 1985; Clark & Reinson, 1990; Shanmugam *et al.*, 2000; Feldman *et al.*, 2008; Feldman &  
680 Demko, 2015) and instead fine-upward like fluvial braid-bars (cf. Ashworth *et al.*, 2011; Reesink  
681 *et al.*, 2014).

682         Conversely, within the MTFR, as tidal-current energy input increases and intrabasinal  
683 wind-waves become relevant, LCR bars exhibit coinciding coarsening and sorting-upward  
684 trends near their bar-tops (between *ca* 1.5 to 0 m depth; Fig. 17B and C). These bar-top  
685 coarsening and sorting-upward sequences are thought to represent the winnowing, or extraction,  
686 of finer sediment (<0.25 mm) at low river-stage from bar-top alluvium via the combined effects  
687 of tidally-produced flood and ebb-currents and intrabasinal wind-waves (cf. Prokocki *et al.*,  
688 2015; Fig. 18A and B). The winnowing of bar-top finer alluvium thus governs the preferential  
689 preservation of moderately well to well-sorted coarser-grained bar-top sediments ( $\geq 0.25$  mm).  
690 The depth within the bar where the coarsening and sorting-upward sequence may appear (Fig.  
691 17B and C), as well as the degree of bioturbation, depends upon the magnitude of wind-wave  
692 energy a bar receives within a given period of time. Bars affected by maximum wind-wave  
693 energy, and thus the largest waves, will have their coarsening and sorting-upward bar-top  
694 sequence begin at greater bar depths, and will lack bioturbation, whilst when wind-wave energy  
695 is weaker, or less frequent, this sequence is initiated at shallower bar depths, but will have a  
696 higher probability of being bioturbated (Fig. 18A and B).

697

698

699

700 **(A) CONCLUSIONS**

701 The present study of mid-channel bars in the fluvial–tidal transition (FTT) of a large mesotidal  
702 river reveals four key findings:

703

704 (1) As a consequence of high-river stage, the sedimentology of FTT bars is dominated by  
705 seaward-directed currents. This causes *ca* 70% of FTT barforms to possess a base to bar-top  
706 sedimentary architecture that is indistinguishable from fluvial braid-bars, whilst  $\geq 80\%$  of the  
707 basal (bar core) strata mimic that of fluvial braid-bars. This suggests that the FTTs of multi-  
708 channelled mesotidal large-rivers (mean annual discharge  $\geq 7000 \text{ m}^3 \text{ s}^{-1}$  and peak discharges  
709  $\geq 15,000 \text{ m}^3 \text{ s}^{-1}$ ) are likely dominated by mid-channel bar strata lacking clearly discerned tidal, or  
710 wind-wave, sedimentological markers.

711

712 (2) Three styles of bar-top Inclined Heterolithic Stratification (IHS) characterize the FTT reach  
713 of the Lower Columbia River (LCR): (i) Fluvially-dominated, tidally-influenced regime, non-  
714 bioturbated low-angle ( $< 5^\circ$ ) to higher-angle ( $> 5^\circ$  to  $\leq 20^\circ$ ) non-cyclic IHS, with fine-grained  
715 interbeds ( $\leq 125 \mu\text{m}$ ) that are deposited by high-river stage sedimentation processes within bartail  
716 and bar-margin accretion-sets, and are indistinguishable from fluvial braid-bar IHS ; (ii) Upper-  
717 mixed tidal–fluvial regime, non-bioturbated low-angle ( $< 5^\circ$ ) cyclic IHS found in mid-bar to  
718 barhead accretion-packages; and (iii) Bioturbated higher-angle ( $> 5^\circ$  to  $\leq 20^\circ$ ) cyclic IHS within  
719 avalanche faces of bartail accretion-units, and low-angle ( $< 5^\circ$ ) cyclic IHS preserved mainly in  
720 mid-bar and barhead accretion-packages. The second and third styles represent a newly  
721 recognized form of IHS in FTT mid-channel barform strata produced by fine sediment that was  
722 deposited initially during high river-stage, but then is re-entrained and redistributed into bar

723 accretion-sets by low river-stage combined-flows consisting of a wind-wave oscillatory-current  
724 and bidirectional tidal-currents. When the wind-wave oscillatory-current of this combined-flow  
725 is relatively weak, or less frequent, IHS within accretion-sets will be more abundant and  
726 bioturbated (i.e. style three).

727

728 (3) When preserved, the second and third styles of upper-mixed tidal–fluvial regime freshwater  
729 IHS provide a distinct sedimentological signature within bar-top strata, which signifies the initial  
730 downstream crossover point in braid-bar architecture from up-dip fully-fluvial (from their bases  
731 to bar-tops), to down-dip facies that possess bar-top depositional fabrics produced by the  
732 hydraulic-sedimentation response of a combined wind wave-tidal influence.

733

734 (4) The dip-angles of IHS within bar-top accretion-packages of LCR freshwater FTT mid-  
735 channel bars are typically  $<5^\circ$ , but can be  $>5^\circ \leq 20^\circ$  when deposited within bartail extension-sets,  
736 and/or bar-margin lateral-accretion units. In contrast, bar-top dip-angles of fluvial, or fluvial-  
737 tidal, point-bar IHS typically range from *ca* 5 to  $15^\circ$ , and remain spatially constant throughout  
738 barhead to bartail accretion-sets. Bar-top IHS of FTT mid-channel bars is therefore more likely  
739 to display lower dip-angles on average that are spatially more variable within a given bar. Thus,  
740 when evaluating the rock record, bar-top IHS with average dip-angles of  $<5^\circ$ , which displays  
741 greater spatial variability, thus provides a diagnostic feature to help determine whether stratal  
742 sequences represent a single-threaded FTT with point-bars *or* a multi-channelled FTT with mid-  
743 channel bars.

744

745

746 **ACKNOWLEDGEMENTS**

747 This research was funded primarily by ExxonMobil, but was also supported by UK Natural  
748 Environment Research Council (NERC) grant awards NE/H007954/1, NE/H006524/1,  
749 NE/H007261/1 and NE/H00582X/1. D.R.P. also acknowledges funding received from the  
750 European Research Council (ERC) under the European Union’s Horizon 2020 research and  
751 innovation program (Grant Agreement 725955). We thank Mike Blum and Howard Feldman for  
752 their advice and insight during this research as well as the Clatsop Community College and  
753 Environmental Research and Training Station for providing space for field instrumentation,  
754 sediment core storage, and access to building equipment and tools. We also thank Kyungsik  
755 Choi, an anonymous reviewer, and Charlie Bristow, for their insightful remarks that strengthened  
756 the final version of this manuscript. A special thank you goes to Michael Wilkin, Katie Rathmell  
757 and António Baptista, for their invaluable advice and expertise regarding the Lower Columbia  
758 River. We also extend thanks to Steve Sandbach, Kyle Balling, and Claire Keevil, for helping  
759 with data collection and, lastly, we thank Pat Killion (captain of the *Tansey Point*) whose many  
760 years of navigational experience along the Lower Columbia River made this research possible.

761

762

763 **REFERENCES**

764

765 **Allen, J.R.L.** (1978) Computational methods for dune time-lag: calculations using Stein's  
766 rule for dune height. *J. Sed. Geol.*, **20(3)**, 165-216.

767

768 **Ashworth, P.J.** (1996) Mid-channel bar growth and its relationship to local flow strength and  
769 direction. *Earth Surf. Proc. Land.*, **21**, 103-123.

770

771 **Ashworth, P.J., Sambrook Smith, G.H., Best, J.L., Bridge, J.S., Lane, S.N., Lunt, I.A.,**  
772 **Reesink, A.J.H., Simpson, C.J. and Thomas, R.E.** (2011) Evolution and sedimentology of a  
773 channel fill in the sandy braided South Saskatchewan River and its comparison to the deposits of  
774 an adjacent compound bar. *Sedimentology*, **58**, 1860-1883.

775

776 **Baker, D., Peterson, C., Hemphill-Haley, E., and Twichell, D.** (2010) Latest Pleistocene and  
777 Holocene (2-16 ka) sedimentation in the Columbia River estuary, Oregon, USA. *Mar.*  
778 *Geol.*, **273**, 83-95.

779

780 **Berné, S., Vagner, P., Guichard, F., Lericolais, G., Liu, Z., Trentesaux, A., Yin, P., and Yi,**  
781 **H.I.** (2002) Pleistocene forced regressions and tidal sand ridges in the East China Sea. *Mar.*  
782 *Geol.*, **30**, 293-315.

783

784 **Best, J.L., Ashworth, P.J., Bristow, C.S. and Roden, J.** (2003) Three-dimensional sedimentary  
785 architecture of a large, mid-channel sand braid bar, Jamuna River, Bangladesh. *J. Sed. Res.*,  
786 **73(4)**, 516-530.

787

788 **Boyd, R., Dalrymple, R.W. and Zaitlin, B.A.** (2006) Estuary and incised valley facies models.  
789 In: *Facies Models Revisited* (Eds H.W. Posamentier and R.G. Walker), *SEPM Spec. Publ.*, **84**,  
790 171-234.

791

792 **Bridge, J.S.** (1993) The interaction between channel geometry, water flow, sediment transport  
793 and deposition in braided rivers. In: *Braided Rivers* (Eds J.L. Best and C.S. Bristow), *Geol. Soc.,*  
794 *London, Special Publication*, **75(1)**, 13-71.

795

796 **Bridge, J.S.** (2006) Fluvial facies models: recent developments. In: *Facies Models Revisited*  
797 (Eds Posamentier, H.W. and Walker, R.G.), Soc. Sed. Geol., Tulsa, OK, *SEPM Spec. Pub.* **84**,  
798 85-170.

799

800 **Bridge, J.S., Collier, R. and Alexander, J.** (1998) Large-scale structure of Calamus River  
801 deposits (Nebraska, USA) revealed using ground-penetrating radar. *Sedimentology*, **45**, 977-986.

802

803 **Bristow, C.S.** (1993) Sedimentary structures exposed in bar tops in the Brahmaputra River,  
804 Bangladesh. In: *Braided Rivers* (Eds J.L. Best and C.S. Bristow), *Geol. Soc., London, Spec.*  
805 *Pub.*, **75(1)**, 277-289.

806

807 **Carling, P.A., Chateau, C.C., Leckie, D.A., Langdon, C.T., Scaife, R.G., and Parsons, D.R.**  
808 (2015) Sedimentology of a tidal point-bar within the fluvial-tidal transition: River Severn

809 Estuary, UK. In: *Fluvial-Tidal Sedimentology* (Eds P.J. Ashworth, J.L. Best and D.R. Parsons),  
810 *Dev. Sedimentol.*, **68**, 149-189.

811

812 **Chaumillon, E., Bertin, X., Falchetto, H., Allard, J., Weber, N., Walker, P., Pouvreau, N.,**  
813 **and Woppelmann, G.** (2008) Multi time-scale evolution of a wide estuary linear sandbank, the  
814 Longe de Boyard, on the French Atlantic coast. *Mar. Geol.*, **251**, 209-223.

815

816 **Chaumillon, E., Fenies, H., Billy, J., Breilh, J.-F., and Richetti, H.** (2013) Tidal and fluvial  
817 controls on the internal architecture and sedimentary facies of a lobate estuarine tidal bar (The  
818 Plassac Tidal Bar in the Gironde Estuary, France). *Mar. Geol.*, **346**, 58-72.

819

820 **Chawla, A., Jay, D.A., Baptista, A.M., Wilkin, M., and Seaton, C.** (2008) Seasonal variability  
821 and estuary-shelf interactions in circulation dynamics of a river-dominated estuary. *Estuar. and*  
822 *Coast.*, **31**, 269-288.

823

824 **Choi, K.** (2010) Rhythmic climbing-ripple cross-lamination in inclined heterolithic stratification  
825 (IHS) of a macrotidal estuarine channel, Gomso Bay, west coast of Korea. *J. Sed. Res.*, **80**, 550-  
826 561.

827

828 **Choi, K.S., Dalrymple, R.W., Chun, S.S., and Kim, S.P.** (2004) Sedimentology of modern,  
829 inclined heterolithic stratification (IHS) in the macrotidal Han River delta, Korea. *J. Sed. Res.*,  
830 **74**, 677-689.

831

832 **Choi, K., Hong, C.M., Kim, M.H., Oh, C.R., and Jung, J.H.** (2013) Morphologic evolution of  
833 macrotidal estuarine channels in Gomso Bay, west coast of Korea: Implications for the  
834 architectural development of inclined heterolithic stratification. *Mar. Geol.*, **346**, 343-354.

835

836 **Clark, J.E. and Reinson, G.E.** (1990) Continuity and performance of an estuarine reservoir,  
837 Crystal Field, Alberta, Canada. In: *Sandstone Petroleum Reservoirs*, Springer, New York, NY,  
838 343-361.

839

840 **Clark, S.M. and Snyder, G.R.** (1969) Timing and extent of flow reversal in the lower Columbia  
841 River. *J. Limnol. Oceanogr.*, **14**, 960-965.

842

843 **Dalrymple, R.W. and Choi, K.** (2007) Morphologic and facies trends through the fluvial-marine  
844 transition in tide-dominated depositional systems: A schematic framework for environmental and  
845 sequence-stratigraphic interpretation. *Earth-Sci. Rev.*, **81**, 135-174.

846

847 **Dalrymple, R.W. and Rhodes, R.N.** (1995) Estuarine dunes and bars. In: *Geomorphology and*  
848 *Sedimentology of Estuaries* (Eds G.M.E. Perillo), *Dev. Sedimentol.*, **53**, 359-422.

849

850 **Dalrymple, R.W., Zaitlin, B.A. and Boyd, R.** (1992) Estuarine facies models: conceptual basis  
851 and stratigraphic implications. *J. Sed. Petrol.*, **62(6)**, 1130-1146.

852

853 **Dalrymple, R.W., Mackay, D.A., Ichaso, A.A., and Choi, K.S.** (2012) Processes,  
854 morphodynamics, and facies of tide-dominated estuaries. In: *Principles of Tidal Sedimentology*  
855 (Eds R.A. Davis Jr. and R.W. Dalrymple), Springer, New York, 79-107.  
856

857 **Dalrymple, R.W., Kurcinka, C.E., Jablonski, B.V.J., Ichaso, A.A. and Mackay, D.A.** (2015)  
858 Deciphering the relative importance of fluvial and tidal processes in the fluvial-marine transition.  
859 In: *Fluvial-Tidal Sedimentology* (Eds P.J. Ashworth, J.L. Best and D.R. Parsons), *Dev.*  
860 *Sedimentol.*, **68**, 3-45.  
861

862 **Durkin, P.R., Hubbard, S.M., Boyd, R.L. and Leckie, D.A.** (2015) Stratigraphic expression of  
863 intra-point-bar erosion and rotation. *J. Sed. Res.*, **85**, 1238-1257.  
864

865 **Fain, A.M.V., Jay, D.A., Wilson, D.J., Orton, P.M. and Baptista, A.M.** (2001) Seasonal and  
866 tidal monthly patterns of particulate matter dynamics in the Columbia River estuary.  
867 *Estuar. and Coast.*, **24(5)**, 770–786.  
868

869 **Feldman, H. and Demko, T.** (2015) Recognition and prediction of petroleum reservoirs in the  
870 fluvial/tidal transition. In: *Fluvial-Tidal Sedimentology* (Eds P.J. Ashworth, J.L. Best and D.R.  
871 Parsons), *Dev. Sedimentol.*, **68**, 483-528.  
872

873 **Feldman, H., Mccrimmon, G. and De Freitas, T.A.** (2008) Fluvial to estuarine valley-fill  
874 models without age-equivalent sandy shoreline deposits, based on the Clearwater  
875 Formation (Cretaceous) at Cold Lake, Alberta, Canada. In: *Recent Advances in Models of*  
876 *Siliciclastic Shallow-marine Stratigraphy, vol. 90* (Eds G.J. Hampson, R.J. Steel, P.M. Burgess  
877 and R.W. Dalrymple), Society for Sedimentary Geology (SEPM), Tulsa, OK, USA, 443-472.  
878

879 **Folk, R.L. and Ward W.C.** (1957) Brazos River bar, a study in the significance of grain-size  
880 parameters. *J. Sediment. Petrol.*, **27**, 3-27.  
881

882 **Fox, D.S., Bell, S., Nehlsen, W. and Damron, J.** (1984) The Columbia River Estuary: atlas of  
883 physical and biological characteristics. *Columbia River Data Development Program (CREDDP)*,  
884 Astoria, OR, 1-87.  
885

886 **Fustic, M., Hubbard, S.M., Spencer, R., Smith, D.G., Leckie, D.A., Bennett, B. and Larter,**  
887 **S.** (2012) Recognition of down-valley translation in tidally influenced meandering fluvial  
888 deposits, Athabasca Oil Sands (Cretaceous), Alberta. Canada. *Mar. Petrol. Geol.*, **29**, 219-232.  
889 **Gelfenbaum, G.** (1983) Suspended-sediment response to semidiurnal and fortnightly tidal  
890 variations in a mesotidal estuary: Columbia River, USA. *Mar. Geol.*, **52**, 39-57.  
891

892 **Gelfenbaum, G., Sherwood, C.R., Peterson, C.D., Kaminsky, G.M., Buijsman, M.,**  
893 **Twichell, D.C., Ruggiero, P., Gibbs, A.E., and Reed, C.** (1999) The Columbia River littoral  
894 cell - a sediment budget overview. In: *Coastal Sediments '99, Long Island, NY, 1999, Proc. Am.*  
895 *Soc. Civ. Eng.*, 1660-1675.  
896

897 **Ghinassi, M., D'alpaos, A., Gasparotto, A., Carniello, L., Brivio, L., Finotello, A., Roner,**  
898 **M., Franceschinis, E., Raldon, N., Howes, N. and Cantelli, A.** (2018) Morphodynamic

899 evolution and stratal architecture of translating tidal point bars: Inferences from the northern  
900 Venice Lagoon (Italy). *Sedimentology*, **65**, 1354-1377.

901

902 **Goodwin, J.L., Emmett, E.W. and Glenne, B.** (1970) Tidal study of three Oregon estuaries.  
903 Engineering Experimental Station, Oregon State University, Bull. No. 45, 1-32.

904

905 **Graf, W.L.** (2006) Downstream hydrologic and geomorphic effects of large dams on American  
906 rivers. *Geomorphology*, **79**, 336-360.

907

908 **Grant, G.E., Schmidt, J.C. and Lewis, S.L.** (2003) A geological framework for interpreting  
909 downstream effects of dams on rivers. In: *A Peculiar River* (Eds J.E. O'Connor and G.E. Grant),  
910 *Water Sci. App.*, **7**, 203-219.

911

912 **Hamilton, P.** (1990) Modelling salinity and circulation for the Columbia River estuary. *Prog.*  
913 *Oceanogr.*, **25**, 113-156.

914

915 **Haushild, W.L.R., Perkins, W., Stevens, H.H., Dempster, G.R., Jr., and Glenn, J.L.** (1966)  
916 Radionuclide transport in the pasco to Vancouver, Washington reach of the Columbia River July  
917 1962 to September 1963. *U.S. Geological Survey Open File*, Portland, OR.

918

919 **Hein, F.J.** (2015) The Cretaceous McMurray oil sands, Alberta, Canada: A world-class, tidally-  
920 influenced fluvial-estuarine system – An Alberta government perspective. In: *Fluvial-Tidal*  
921 *Sedimentology* (Eds P.J. Ashworth, J.L. Best and D.R. Parsons), *Dev. Sedimentol.*, **68**, 561-621.

922

923 **Herrman, R.B.** (1972) *The distribution and abundance of clams in Grays Harbor as related to*  
924 *environmental conditions, summary report [unpub.]*, Longview, Washington, Weyerhaeuser Co.

925

926 **Hickson, R. E.** (1912) A report on the establishment of river gauges on lower Columbia River &  
927 Willamette Rivers. *Army Corps of Engineers*, 1-8.

928

929 **Hoitink, A.J.F. and Jay, D.A.** (2016) Tidal river dynamics: Implications for deltas. *Rev.*  
930 *Geophys.*, **54**, 240-272.

931

932 **Horner-Devine, A.R., Jay, D.A., Orton, P.M., and Spahn, E.Y.** (2009) A conceptual model of  
933 the strongly tidal Columbia River plume. *J. of Mar. Syst.*, **78**, 460-475.

934

935 **Hubbard, S.M., Smith, D.G., Nielsen, H., Leckie, D.A., Fustic, M., Spencer, R.J. and Bloom,**  
936 **L.** (2011) Seismic geomorphology and sedimentology of a tidally influenced river deposit,  
937 Lower Cretaceous Athabasca oil sands, Alberta, Canada. *AAPG Bull.*, **95(7)**, 1123-1145.

938

939 **Jablonski, B.V.J. and Dalrymple, R.W.** (2016) Recognition of strong seasonality and climatic  
940 cyclicity in an ancient, fluvially dominated, tidally influenced point bar: Middle McMurray  
941 Formation, Lower Steepbank River, north-eastern Alberta, Canada. *Sedimentology*, **63**, 552-585.

942

943 **Jay, D.A.** (1984) Circulatory processes in the Columbia River Estuary. CREST, Astoria,  
944 Oregon, 1-169.

945 **Jay, D.A.** (2009) Evolution of tidal amplitudes in the eastern Pacific Ocean. *Geophys. Res. Lett.*,  
946 **36**, LO4603, doi:10.1029/2008GL036185.

947

948 **Jay, D.A.** and **Naik, P.K.** (2011) Distinguishing human and climate influences on hydrological  
949 disturbance processes in the Columbia River, USA. *Hydrolog. Sci. J.*, **56**, 1186-1209.

950

951 **Jay, D.A., Giese, B.S.** and **Sherwood, C.R.** (1990) Energetics and sedimentary processes in the  
952 Columbia River Estuary. *Prog. Oceanogr.*, **25**, 157-174.

953

954 **Jay, D.A., Leffler, K.** and **Degens, S.** (2011) Long-term evolution of Columbia River tides. *J.*  
955 *Waterway, Port, Coastal, and Ocean Eng.*, **137(4)**, 182-191.

956

957 **Johnson, J.W.** (1972) Tidal inlets on the California, Oregon, and Washington coasts. Hydraulic  
958 Engineering Laboratory, University of California, Berkeley, *Technical Report HEL 24-12*.

959

960 **Johnson, S.M.** and **Dashtgard, S.E.** (2014) Inclined heterolithic stratification in a mixed tidal-  
961 fluvial channel: Differentiating tidal versus fluvial controls on sedimentation. *Sed. Geol.*, **301**,  
962 41-53.

963

964 **Knotts, N.P.** and **Barrick, R.C.** (1976) Hydrodynamics of Grays Harbor estuary, Washington:  
965 Appendix A. In: *Maintenance dredging and the environment of Grays Harbor, Washington*. U.S.  
966 Army Engineer District, Seattle, Washington, 1-95.

967

968 **Kukulka, T.** and **Jay, D.A.** (2003) Impacts of Columbia River discharge on salmonoid habitat:  
969 1. A nonstationary fluvial tide model. *J. Geophys. Res.*, **108(C9)**, 3293,  
970 doi:10.1029/2002JC001382.

971

972 **Leeder, M.** and **Bridges, P.H.** (1975) Flow separation in meander bends. *Nature*, **253**, 338-339.

973

974 **Leuven, J.R.F.W., Kleinans, M.G., Weisscher, S.A.H.** and **van der Vegt, M.** (2016) Tidal  
975 sand bar dimensions and shapes in estuaries. *Earth-Sci. Rev.*, **161**, 204-223.

976

977 **Losada, M.A., Díez-Minguito, M.** and **Reyes-Merlo, M.Á.** (2017) Tidal-fluvial interaction in  
978 the Guadalquivir River Estuary: Spatial and frequency-dependent response of currents and water  
979 levels. *J. Geophys. Res. Oceans*, **122**, 847-865.

980

981 **Martinius, A.W.** and **Van den Berg, J.H.** (2011) *Atlas of sedimentary structures in estuarine*  
982 *and tidally-influenced river deposits of the Rhine-Meuse-Scheldt system: their application to*  
983 *the interpretation of analogous outcrop and subsurface depositional systems*. EAGE  
984 Publications, Houten, The Netherlands, 298 pp.

985

986 **Martinius, A.W., Jablonski, B.V.J., Fustic, M., Strobl, R.** and **Van den Berg, J.H.** (2015)  
987 Fluvial to tidal transition zone facies in the McMurray Formation (Christina River, Alberta,  
988 Canada), with emphasis on the reflection of flow intensity in bottomset architecture. In: *Fluvial-*  
989 *Tidal Sedimentology* (Eds P.J. Ashworth, J.L. Best and D.R. Parsons), *Dev. Sedimentol.*, **68**, 445-  
990 480.

- 991 **Moreton, D.J. and Carter, B.J.** (2015) Characterizing alluvial architecture of point bars within  
992 the McMurray Formation, Alberta, Canada, for improved bitumen resource prediction and  
993 recovery. In: *Fluvial-Tidal Sedimentology* (Eds P.J. Ashworth, J.L. Best and D.R. Parsons), *Dev.*  
994 *Sedimentol.*, 68, 529-559.
- 995  
996 **Mumpy, A.J., Jol, H.M., Kean, W.F. and Isbell, J.L.** (2007) Architecture and sedimentology  
997 of an active braid bar in the Wisconsin River based on 3-D ground penetrating radar. In:  
998 *Stratigraphic Analysis Using GPR* (Eds G.S. Barker and H.M. Jol), *Geol. Soc. Am. Spec. Pap.*  
999 *432*, 111-131.
- 1000  
1001 **Mutti, E., Rosell, J., Allen, G.P., Fonnesu, F. and Sgavetti, M.** (1985) The Eocene Baronia  
1002 tide dominated delta-shelf system in the Ager Basin. In: *Excursion Guidebook: 6th*  
1003 *International Association of Sedimentologists European Regional Meeting*, 577-600.
- 1004  
1005 **Naik, P.K. and Jay, D.A.** (2005) Estimation of Columbia River virgin flow: 1879 to 1928.  
1006 *Hydrol. Process.*, 19, 1807-1824.
- 1007  
1008 **Naik, P.K. and Jay, D.A.** (2011) Distinguishing human and climate influences on the Columbia  
1009 River: Changes in mean flow and sediment transport. *J. Hydrol.*, 404, 259-277.
- 1010  
1011 **Nanson, G.C., and Page, K.J.** (1983) Lateral accretion of fine-grained concave benches on  
1012 meandering rivers. In: *Modern and Ancient Fluvial Systems* (Eds D.J. Collinson and J. Lewin),  
1013 *Int. Assoc. Sedimentol. Spec. Publ. 6*, 133-143.
- 1014  
1015 **Parker, N.O., Sambrook Smith, G.H., Ashworth, P.J., Best, J.L., Lane, S.N., Lunt, I.A.,**  
1016 **Simpson, C.J. and Thomas, R.E.** (2013) Quantification of the relation between surface  
1017 morphodynamics and subsurface sedimentological product in sandy braided rivers.  
1018 *Sedimentology*, 60, 820-839.
- 1019  
1020 **Percy, K.L., Sutterlin, C., Bella, D.A. and Klingeman, P.C.** (1974) Oregon's Estuaries: Sea  
1021 Grant College Program. Oregon State University, Corvallis, 1-294.
- 1022  
1023 **Peterson, C., Scheidegger, K., Komar, P. and Niem, W.** (1984) Sediment composition and  
1024 hydrography in six high-gradient estuaries of the northwestern United States. *J. Sed. Petrol.*, 54,  
1025 86-97.
- 1026  
1027 **Peterson, C.D., Gates, E.B., Minor, R. and Baker, D.L.** (2013) Accommodation space controls  
1028 on the latest Pleistocene and Holocene (16-0 ka) sediment size and bypassing in the lower  
1029 Columbia River valley: a large fluvial-tidal system in Oregon and Washington, USA.  
1030 *J. Coast. Res.*, 29 (5), 1191-1211.
- 1031  
1032 **Peterson, C., Vanderburgh, S., and Roberts, M.C.** (2014) Late Holocene geomorphology of  
1033 the Columbia River estuary, Oregon and Washington, USA. *J. Geogr. Geol.*, 6(2), 1-27.
- 1034  
1035 **Prokocki, E.W., Best, J.L., Ashworth, P.J., Parsons, D.R., Sambrook Smith G.H., Nicholas,**  
1036 **A.P., Simpson, C.J., Wang, H., Sandbach, S.D. and Keevil, C.E.** (2015) Mid to late Holocene

1037 geomorphological and sedimentological evolution of the fluvial-tidal zone: Lower Columbia  
1038 River, WA/OR, USA. In: *Fluvial-Tidal Sedimentology* (Eds P.J. Ashworth, J.L. Best and D.R.  
1039 Parsons), *Dev. Sedimentol.*, **68**, 193-226.

1040

1041 **Reesink, A.J.H., Ashworth, P.J., Sambrook Smith, G.H., Best, J.L., Parsons, D.R., Amsler,**  
1042 **M.L., Hardy, R.J., Lane, S.N., Nicholas, A.P., Orfeo, O., Sandbach, S.D., Simpson, C.J. and**  
1043 **Szupiany, R.N.** (2014) Scales and causes of heterogeneity in bars in a large multi-channel river:  
1044 Río Paraná, Argentina. *Sedimentology*, **61**, 1055-1085.

1045

1046 **Reijnenstein, H.M., Posamentier, H.W. and Bhattacharya, J.P.** (2011) Seismic geomorphology  
1047 and high-resolution seismic stratigraphy of inner-shelf fluvial, estuarine, deltaic, and marine  
1048 sequences, Gulf of Thailand. *AAPG Bull.*, **95(11)**, 1959-1990.

1049

1050 **Rubin, D.M., Topping, D.J., Schmidt, J.C., Hazel, J., Kaplinski, M. and Melis, T.S.** (2002)  
1051 Recent sediment studies refute Glen Canyon Dam hypothesis. *EOS*, **83(25)**, 273-278.

1052

1053 **Sambrook Smith, G.H., Ashworth, P.J., Best, J.L., Woodward, J. and Simpson, C.J.** (2006)  
1054 The sedimentology and alluvial architecture of the sandy braided South Saskatchewan River,  
1055 Canada. *Sedimentology*, **53**, 413-434.

1056

1057 **Sambrook Smith, G.H., Ashworth, P.J., Best, J.L., Lunt, I.A., Orfeo, O. and Parsons, D.R.**  
1058 (2009) The sedimentology and alluvial architecture of a large braid bar, Río Paraná, Argentina. *J.*  
1059 *Sed. Res.*, **79**, 629-642.

1060

1061 **Sandbach, S.D., Nicholas, A.P., Ashworth, P.J., Best, J.L., Keevil, C.E., Parsons, D.R.,**  
1062 **Prokocki, E.W. and Simpson, C.J.** (2018) Hydrodynamic modelling of tidal-fluvial flows in a  
1063 large river estuary. *Estuar. Coast. Shelf. Sci.*, **212**, 176-188.

1064

1065 **Schmidt, J.C. and Graf, B.** (1990) Aggradation and degradation of alluvial-sand deposits, 1965  
1066 to 1986, Colorado River, Grand Canyon National Park, Arizona. *USGS Prof. Pap.* **1493**.

1067

1068 **Seminara G., Lanzoni S., Pittaluga M.B. and Solari, L.** (2001) Estuarine patterns: an  
1069 introduction to their morphology and mechanics. In: *Geomorphological Fluid Mechanics* (Eds  
1070 N.J. Balmforth and A. Provenzale), *Lecture Notes in Physics*, **582**, Springer, Berlin, Heidelberg.

1071

1072 **Shanley, K.W., McCabe, P.J. and Hettlinger, R.D.** (1992) Tidal influence in Cretaceous fluvial  
1073 strata from Utah, USA: a key to sequence stratigraphic interpretation. *Sedimentology*, **39**, 905-  
1074 930.

1075

1076 **Shanmugam, G., Poffenberger, M. and Toro Alava, J.** (2000) Tide-dominated estuarine facies  
1077 in the Hollin and Napo. *AAPG Bull.*, **84(5)**, 652-682.

1078

1079 **Sherwood, C.R. and Creager, J.S.** (1990) Sedimentary geology of the Columbia River Estuary.  
1080 *Prog. Oceanogr.*, **25**, 15-79.

1081

1082 **Sherwood, C.R., Jay, D.A., Harvey, R.B., Hamilton, P. and Simenstad, C.A.** (1990)  
1083 Historical changes in the Columbia River Estuary. *Prog. Oceanogr.*, **25**, 299-352.  
1084

1085 **Simenstad, C.A., Burke, J.L., O'Connor, J.E., Cannon, C., Heatwolve, D.W., Ramiez, M.F.,**  
1086 **Waite, I.R., Counihan, T.D. and Jones, K.L.** (2011) Columbia River estuary ecosystem  
1087 classification—concept and application. U.S. Geological Survey, open-file report  
1088 2011-1228, Reston, 1-54.  
1089

1090 **Sisulak, C.F. and Dashtgard, S.E.** (2012) Seasonal controls on the development and character  
1091 of inclined heterolithic stratification in a tide-influenced, fluvially dominated channel: Fraser  
1092 River, Canada. *J. Sed. Res.*, **82**, 244-257.  
1093

1094 **Smith, D.G.** (1987) Meandering river point bar lithofacies models: modern and ancient  
1095 examples compared. In: *Recent Developments in Fluvial Sedimentology* (Eds F.G. Ethridge,  
1096 R.M. Flores and M.D. Harvey), *Soc. Econ. Paleontol. Mineral. Spec. Publ.*, **39**, 83-91.  
1097

1098 **Smith, D.G.** (1988) Tidal bundles and mud couplets in the McMurray Formation, northeastern  
1099 Alberta, Canada. *Bull. Can. Petrol. Geol.*, **36**, 216-219.  
1100

1101 **Smith, D.G.** (1989) Comparative sedimentology of mesotidal (2 to 4 m) estuarine channel point  
1102 bar deposits from modern examples and ancient Athabasca Oil Sands (Lower Cretaceous),  
1103 McMurray Formation. In: *Modern and Ancient Examples of Clastic Tidal Deposits – Core and*  
1104 *Peel Workshop* (Eds G.E. Reinson), *Can. Soc. Petrol. Geol.*, Second International Research  
1105 Symposium on Clastic Tidal Deposits, 60-65.  
1106

1107 **Smith, D.G., Hubbard, S.M., Leckie, D.A. and Fustic, M.** (2009) Counter point-bar deposits:  
1108 lithofacies and reservoir significance in the meandering modern Peace River and ancient  
1109 McMurray Formation, Alberta, Canada. *Sedimentology*, **56**, 1655-1669.  
1110

1111 **Smith, D.G., Hubbard, S.M., Lavigne, J.R., Leckie, D.A. and Fustic, M.** (2011) Stratigraphy  
1112 of counter-point-bar and eddy-accretion deposits in low-energy meander belts of the Peace-  
1113 Athabasca Delta, northeast Alberta, Canada. In: *From River to Rock Record: The Preservation of*  
1114 *Fluvial Sediments and Their Subsequent Interpretation* (Eds S. Davidson, S. Leleu and C.P.  
1115 North), *SEPM Spec. Publ.*, **97**, 143-152.  
1116

1117 **Stolz, A., Martin, C. and Wong, C.** (2005) Vertical control in a tidally influenced complex river  
1118 system with a fixed low water datum. *Hydrographic Society of America Meeting*, 20-31.  
1119

1120 **Templeton, W.J. and Jay, D.A.** (2013) Lower Columbia River sand supply and removal:  
1121 estimates of two sand budget components. *J. Water. Port Ocean Eng.*, **139(5)**, 383-392.  
1122

1123 **Thomas, R.G., Smith, D.G., Wood, J.M., Visser, J., Calverley-Range, E.A. and Koster, E.H.**  
1124 (1987) Inclined heterolithic stratification – terminology, description, interpretation and  
1125 significance. *Sed. Geol.*, **53**, 123-179.  
1126

1127 **Topping, D. J., Rubin, D. M. and Vierra Jr., L. E.** (2000a) Colorado River sediment transport.  
1128 1. Natural sediment supply limitation and the influence of Glen Canyon Dam. *Wat. Resour. Res.*,  
1129 **36(2)**, 515-542.  
1130

1131 **Topping, D. J., Rubin, D. M., Nelson, J. M., Kinzel III, P. J. and Corson, I. C.** (2000b)  
1132 Colorado River sediment transport. 2. Systematic bed-elevation and grain-size effects of sand  
1133 supply limitation. *Wat. Resour. Res.*, **36(2)**, 543-570.  
1134

1135 **Utt, M.E.** (1975) *Seasonal variations in tidal dynamics, water quality and sediments in the*  
1136 *Siuslaw Estuary. [M.Sc. thesis].* Oregon State University, 76 pp.  
1137

1138 **Van de Lageweg, W.I. and Feldman, H.** (2018) Process-based modelling of morphodynamics  
1139 and bar architecture in confined basins with fluvial and tidal currents. *Mar. Geol.*, **398**, 35-47.  
1140

1141 **Van de Lageweg, W.I., Braat, L., Parsons, D.R. and Kleinhans, M.G.** (2018) Controls on  
1142 mud distribution and architecture along the fluvial-to-marine transition. *Geology*, **46**, 971-974.  
1143

1144 **Van den Berg, J.H., Boersma, J.R. and Van Gelder, A.** (2007) Diagnostic sedimentary  
1145 structures of the fluvial-tidal transition zone: evidence from deposits of the Rhine Delta. *Nether.*  
1146 *J. Geosci.*, **86(3)**, 287-306.  
1147

1148 **Walton, Jr., T.L. and Adams, W.D.** (1976) Capacity of inlet outer bars to store sand. *Proc. Am.*  
1149 *Soc. Civ. Eng. Part II: Coastal Sediment Problems*, 1919-1937.  
1150

1151 **Wightman, D.M. and Pemberton, S.G.** (1997) The Lower Cretaceous (Aptian) McMurray  
1152 Formation: an overview of the Fort McMurray area, northeastern Alberta. In: *Petroleum Geology*  
1153 *of the Cretaceous Mannville Group, Western Canada* (Eds S.G. Pemberton and D.P. James),  
1154 *Can. Soc. Petrol. Geol. Mem.*, **18**, 312–344.  
1155

1156 **Wightman, D.M., Strobl, R.S., Cotterill, D.K., Berhane, H., and Attalla, M.N.** (1997)  
1157 Stratigraphy, depositional modelling and resource characterization of the McMurray/Wabiskaw  
1158 deposit, western portion of the Athabasca oil sands area, northeastern Alberta. In: *Petroleum*  
1159 *Geology of the Cretaceous Mannville Group, Western Canada* (Eds S.G. Pemberton and D.P.  
1160 James), *Can. Soc. Petrol. Geol. Mem.*, **18**, 345-374.

1161 **Williams, G.P. and Wolman, M.G.** (1984) Downstream effects of dams on alluvial rivers.  
1162 *USGS Prof. Pap. 1286*, Washington, D.C.

1163 **Yalin, M.S.** (1964) Geometrical properties of sand waves. *J. Hydraul. Eng.*, **90(5)**, 105–119.  
1164  
1165

1166

1167

**TABLE LEGEND**

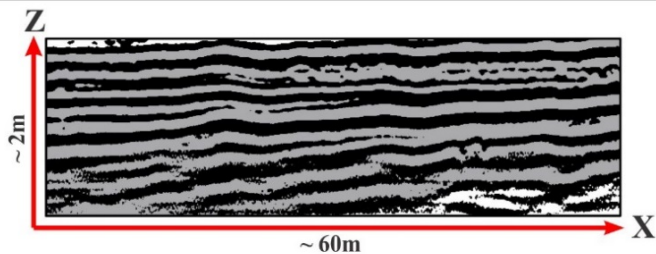
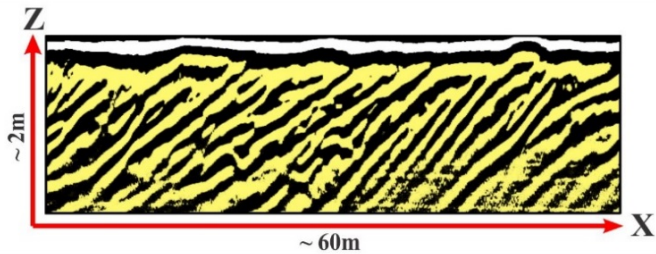
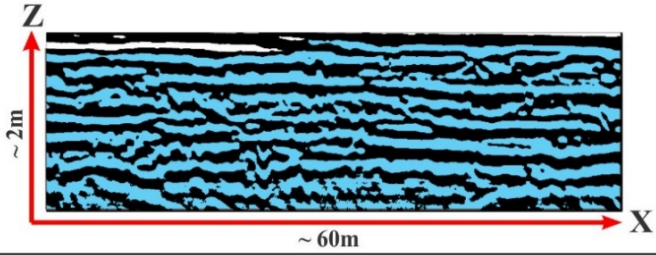
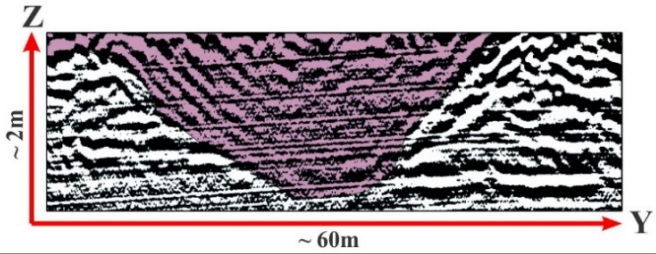
	Grays Harbor/Chehalis River	Tillamook Bay	Siuslaw River	Alesea River	Siletz River	Lower Columbia River
mean annual fluvial discharge, $Q_{Wavg}$ , at mouth ( $m^3s^{-1}$ )	320 (b)	60 (f)	89 (f)	43 (f)	55 (f)	7,300 (h)
mean diurnal tidal prism, $Q_{tide}$ , at mouth ( $m^3$ )	$6.0 \times 10^8$ (e)	$6.1 \times 10^7$ (d)	$1.0 \times 10^7$ (f)	$1.4 \times 10^7$ (a)	$9.9 \times 10^6$ (a)	$11.0 \times 10^8$ (c)
mean range of tide at, or near, mouth (m)	2.2 (e)	1.7 (d)	1.6 (i)	1.8 (a)	1.5 (d)	1.7 (j)
mean hydrographic ratio ( $H_g$ )	86 (g)	47 (g)	5 (g)	15 (g)	8 (g)	7

1169  
 1170  
 1171  
 1172  
 1173  
 1174  
 1175  
 1176  
 1177  
 1178  
 1179  
 1180

- (a) Goodwin *et al.* (1970)
- (b) Hermann (1972)
- (c) Walton & Adams (1976)
- (d) Johnson (1972)
- (e) Knotts & Barrick (1976)
- (f) Percy *et al.* (1974)
- (g) Peterson *et al.* (1984)
- (h) Naik & Jay (2011)
- (i) Utt (1975)
- (j) Simenstad *et al.* (2011)

1181 **Table 1.** Comparison of modern fluvio-tidal characteristics and hydrographic ratios ( $H_g$ ) of  
 1182 rivers and tidal-bays located along the central Cascadia Margin, USA. Note  $H_g =$   
 1183  $(Q_{tide}/Q_{Wavg}) \times 6 \text{ hrs}$  (half a tidal-cycle), and that values of  $H_g < 10$  represent systems that are  
 1184 fluvially, or ebb-tidal, dominant. Modified from Peterson *et al.* (1984).  
 1185

1186  
 1187  
 1188  
 1189  
 1190  
 1191

Radar facies	Facies description	Facies scale	Facies examples
1	Upper-subtidal to intertidal vertically stacked, laterally- and longitudinally-continuous, low-angle (< 5°, but typically 1-2°) reflectors with high amplitude. Commonly forms near bar-tops (0-5m depth).	Up to 4-5m thick, and can extend to ≤ 500m in longitudinal (x) and lateral (y) directions	
2	Subtidal to intertidal laterally- or longitudinally- continuous sets of high-angle inclined reflectors that are > 6°, but are commonly < 20°. This facies tends to grade laterally or longitudinally into facies 1 or 3, and may display a range of dip-angles and amplitudes.	Commonly 1-2m thick, but can be up to 4m in thickness, and extends ~ 30-100m in x- or y- directions	
3	Mainly subtidal, but can be intertidal, vertically stacked undular, discontinuous, or chaotic, reflectors inclined at < 6°. However, parallel reflectors commonly bound the base and tops of trough-shaped reflectors of varying thicknesses and dip-angles.	Stacked-sets can be up to 8m thick, but individual sets are usually 0.25-1m thick. May extend 100s m in x- and y- directions	
4	Typically intertidal, but can be subtidal, concave reflectors, with vertically stacked reflectors of variable dip within. This facies always has a strong concave reflector at its base that adjacent reflectors terminate against.	Usually ~ 4m thick, but can be minimally 1-2m in thickness, and extends 20-100m in y- direction	

1192

1193

1194

1195

**Table 2.** Ground penetrating radar (GPR) reflector facies descriptions and examples captured in LCR mid-channel barform profiles. See main text for specific FTT hydraulic regime sedimentological descriptions and interpretations.

Sedimentary Log and GPR-Profile Key	
<b>Sedimentary Structures</b>	
	- Cross-bedding (i.e. dune-scale)
	- Cross-laminae (i.e. current-ripples)
	- Low-angle truncations
	- Planar laminae
	- Silt/very-fine sand drape and/or heterogeneous bedding with no distinct layering between silt/very-fine sands and fine to med sands
	- Fining-upwards sequence
	- Coarsening-upwards sequence
	- Pumice Clasts
	- Interbed of mixed macroscopic plant/organic detritus and pumice clasts
	- Macroscopic plant/organic debris
	- Homogeneous/structureless bedding generated during core extraction and/or transport
	- Erosional contact
	- Intensely bioturbated horizon with no original bedding structure preserved
	- Sorting-upwards sequence
<b>Folk Grain Sorting Index</b>	
	0.35-0.50 well-sorted
	0.50-0.71 moderately well-sorted
	0.71-1.0 moderately sorted
	1.0-2.0 poorly sorted
	2.0-4.0 very-poorly sorted
<b>Tidal/Wind Elevation Markers</b>	
	= Mean Higher-High Water - The average of the higher-high water height of each tidal day observed over the national tidal datum epoch 1983-2001
	= Mean Sea Level - The arithmetic mean of hourly heights observed over the national tidal datum epoch 1983-2001
	= Mean Lower-Low Water - The average of the lower-low water height of each tidal day observed over the national tidal datum epoch 1983-2001
	= Potential maximum depth from the MHHW level that intrabasinal wind-waves can re-suspend sediments <= medium sands
	= Potential maximum depth from the MLLW level that intrabasinal wind-waves can re-suspend sediments <= medium sands

1196

1197

1198 **Table 3.** Key to vibracore sedimentary logs and GPR cross-sectional profiles. The Mean Higher-

1199 High Water (MHHW), Mean Sea Level (MSL), and Mean Lower-Low Water (MLLW) levels

1200 displayed on each log and GPR-profile were determined from Stolz *et al.* (2005). Note that the

1201 potential maximum depths of LCR intrabasinal wind-wave sediment resuspension (MaxW1 and

1202 MaxW2) are from Peterson *et al.* (2014).

1203

1204

1205

1206

1207

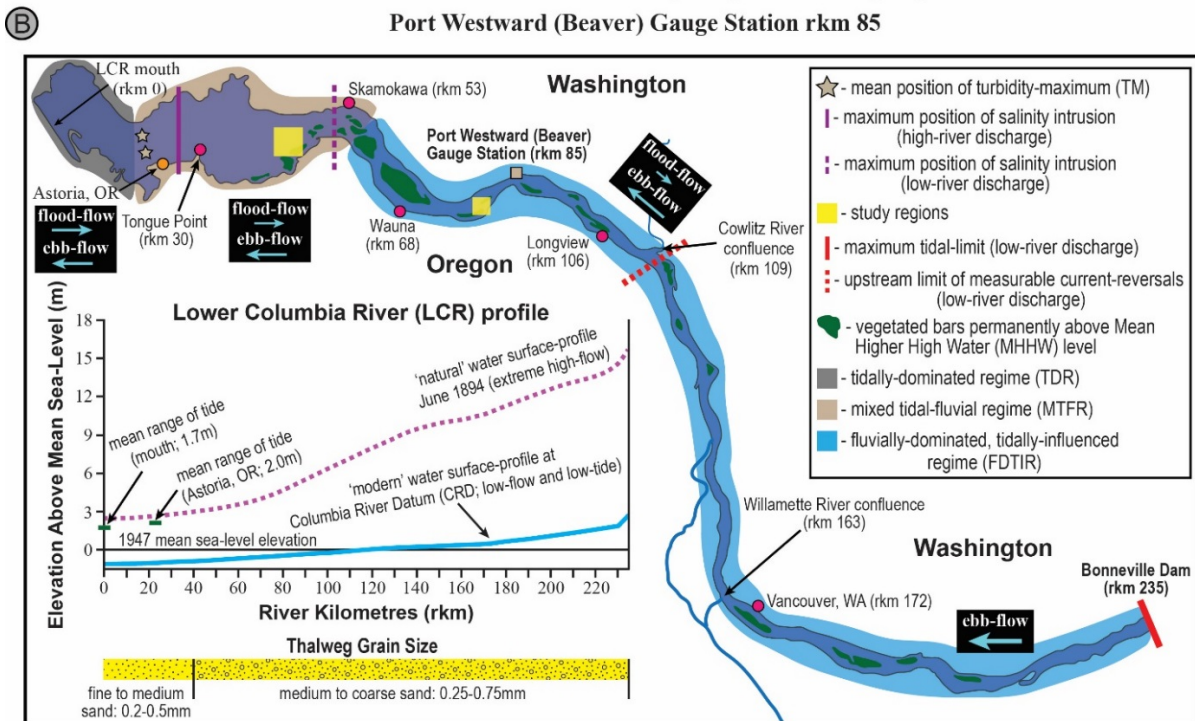
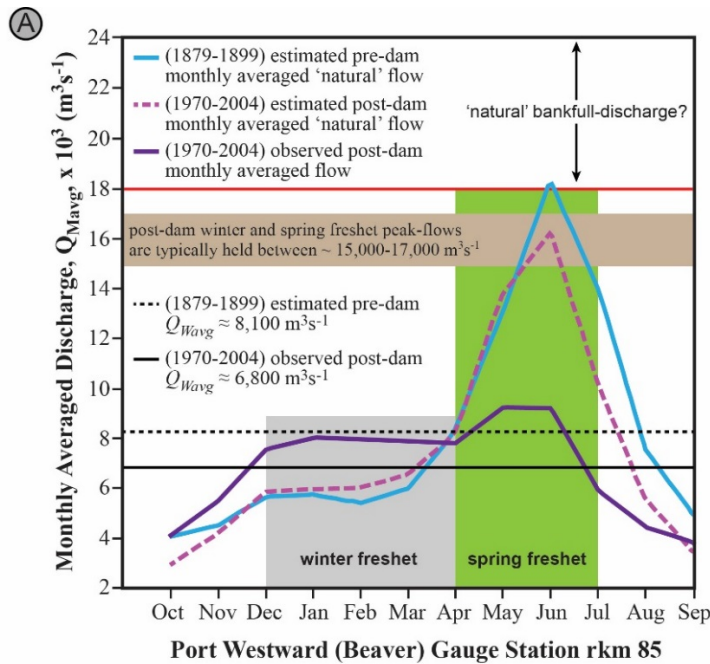




1226

1227

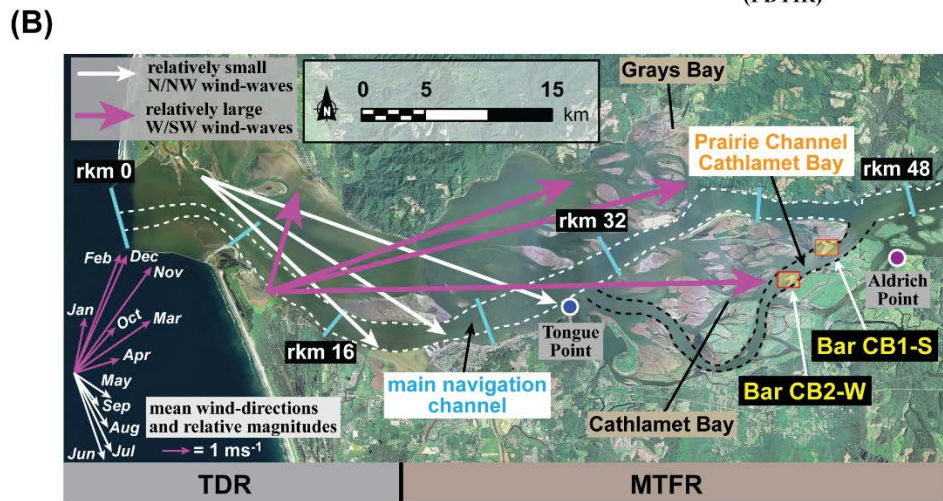
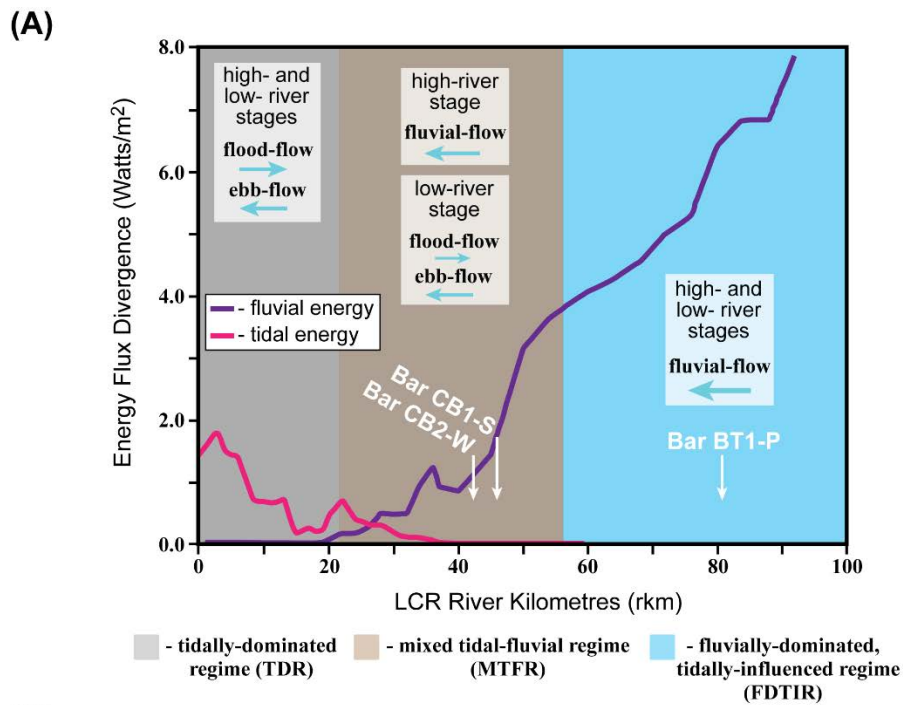
1228 **Figure 2.** (A) Aerial image of the lower Columbia River (LCR) study reach displaying the mean  
 1229 boundaries of the fluvial–tidal transition hydraulic regimes as defined by Jay *et al.* (1990) as well  
 1230 as the outline of the main navigation channel (dashed white line). Included are the positions of  
 1231 the three mid-channel barforms investigated herein (yellow rectangles), the longitudinal channel  
 1232 extent of salinity intrusion during high and low-fluvial flows as reported by Fox *et al.* (1984) and  
 1233 Chawla *et al.* (2008), the average position of the LCR turbidity-maximum (green stars) at *ca* rkm  
 1234 21 (Jay *et al.*, 1990), and the location of the Beaver (Port Westward) gauge station at rkm 85. (B)  
 1235 to (D) magnified images of the three bars analysed herein displaying the locations where ground  
 1236 penetrating radar (GPR) transects (yellow lines) and sediment cores (pink circles) were collected.  
 1237 Aerial imagery from US National Agriculture Imagery Program (NAIP) at  
 1238 <https://gdg.sc.egov.usda.gov/>.



1239

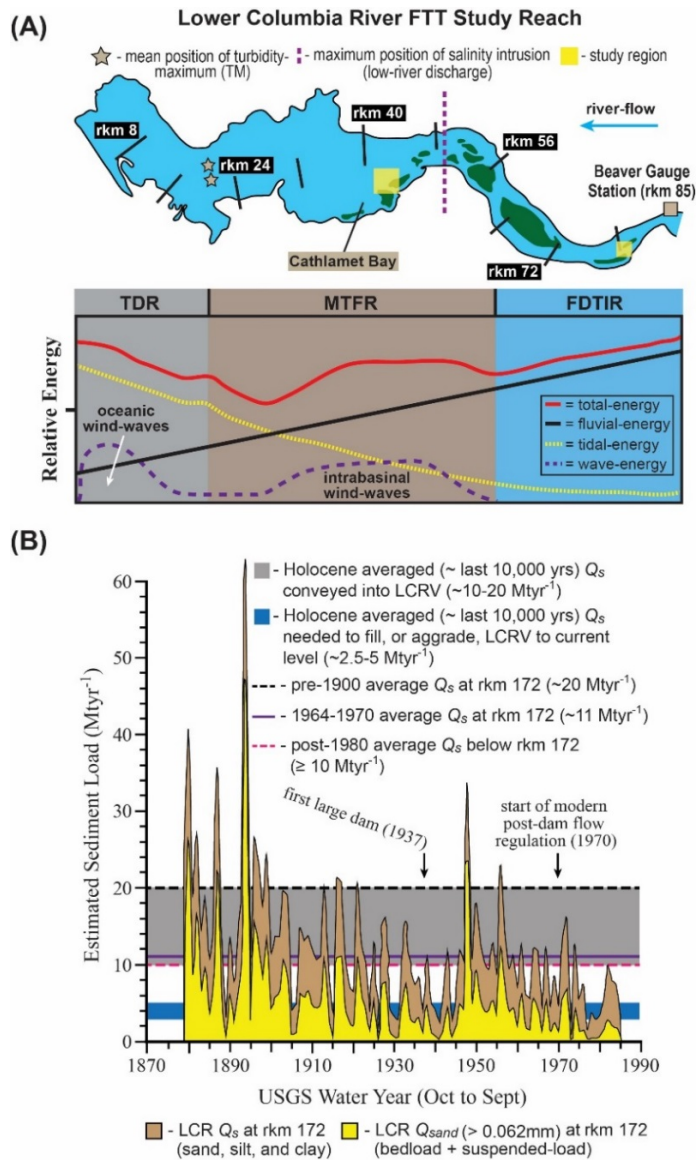
1240

1241 **Figure 3.** (A) Monthly averaged ‘natural’ Lower Columbia River (LCR) discharge (1879 to  
 1242 1899; blue line) *versus* monthly averaged irrigation depleted and dam regulated modern LCR  
 1243 discharge (1970 to 2004; purple line) at the Port Westward (Beaver) gauge station at rkm 85  
 1244 positioned at the upstream boundary of study reach. Modified from Naik & Jay (2011). (B)  
 1245 Planform diagram of the LCR from rkm 0 to 235 displaying the boundaries of its FTT regimes as  
 1246 well as the limits and positions of pertinent tidal-characteristics. Also shown is: (i) the modern  
 1247 LCR water surface profile from rkm 0 to 235 at extreme high-river flow and at low-river flow  
 1248 and low-tide; and (ii) thalweg grain-size range.



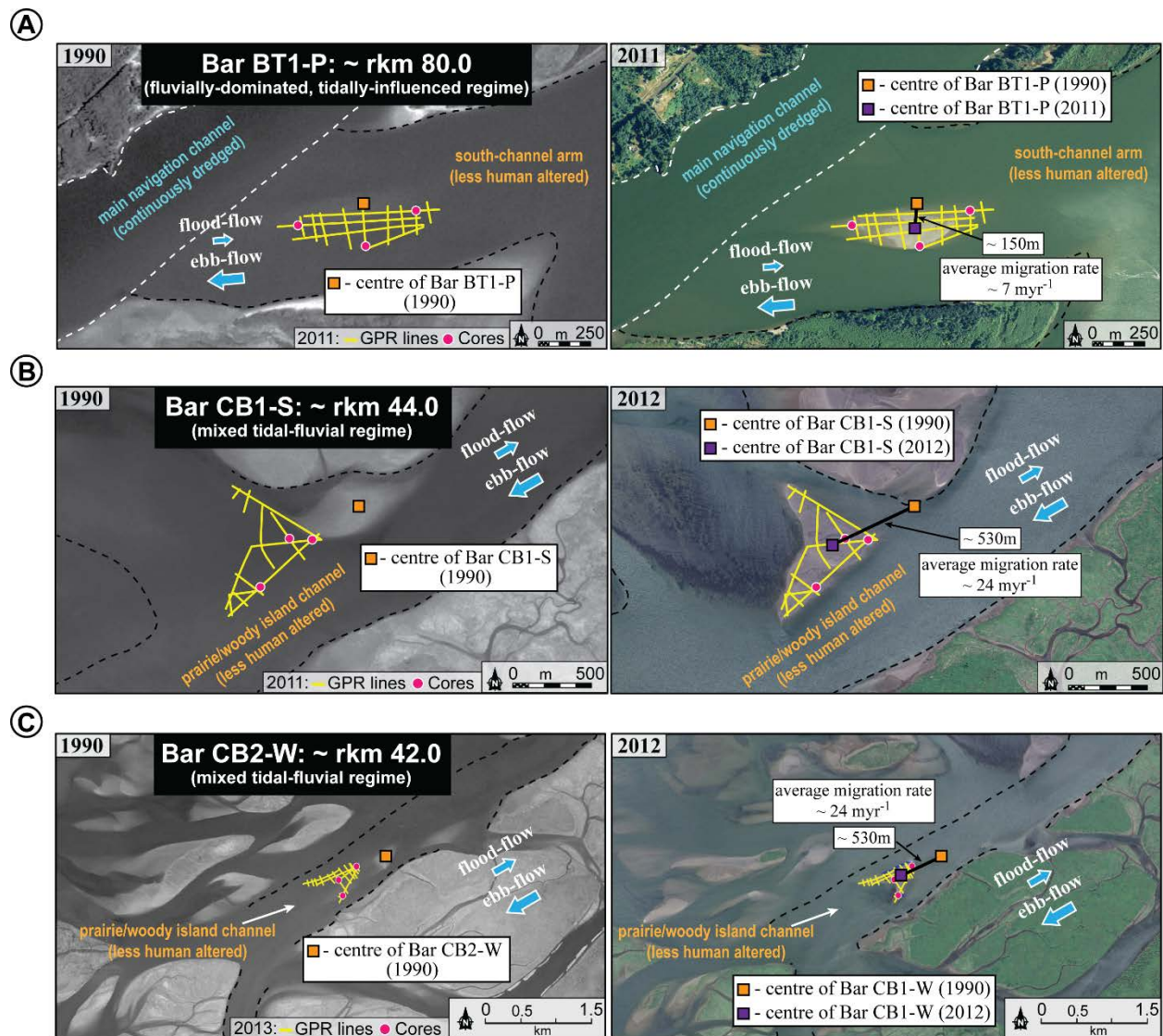
1249  
1250  
1251  
1252  
1253  
1254  
1255  
1256  
1257  
1258  
1259  
1260  
1261  
1262  
1263

**Figure 4.** (A) Long-term mean energy flux divergence of Lower Columbia River (LCR) tidal (pink line) versus fluvial (purple line) hydraulic sources as computed by Giese & Jay (1989) and Jay *et al.* (1990). Note that flux values represent the amount of tidal or fluvial potential energy sourced through channel cross-sections at each LCR rkm as measured by Jay (1984). (B) Annual LCR intrabasinal wind-wave directions and magnitudes relative to the positions of Bars CB1-S and CB2-W. Note, however, that the image displayed was taken when water-levels were below the Mean Lower Low Water (MLLW) mark, and that the normal condition is for almost all barforms displayed to be submerged when the water surface is higher than MLLW (see fig. 6.1, Prockocki *et al.*, 2015). The largest wind-waves (pink arrows) are generated over the longest fetch length between January to April and in October and November, and are oriented from the west/south-west to east/north-east, whilst smaller wind-waves (white arrows) are produced from May to September, and are oriented from north/north-west to south/south-east. Wind data from Peterson *et al.* (2014).



1264

1265 **Figure 5.** (A) Temporally averaged relative energy diagram for the Lower Columbia River  
 1266 (LCR) fluvial–tidal transition (FTT) study reach investigated. The mixed tidal–fluvial regime  
 1267 (MTFR) (Bars CB1-S and CB2-W) is mainly subjected to fluvial-currents during moderate to  
 1268 high-river stages, but at low-river stage will experience combined-flows composed of fluvial-  
 1269 and/or tidal- currents and intrabasinal wind-wave oscillatory-currents. Next, within the fluvially-  
 1270 dominated, tidally-influenced regime (FDTIR) (Bar BT1-P), sediment transport is primarily  
 1271 dictated by fluvial-currents as the result of moderate to high-river stages. This diagram is based  
 1272 from the results of Jay *et al.* (1990) and Peterson *et al.* (2014). (B) Hindcast estimates (1879 to  
 1273 1985) of LCR mean annual sediment load ( $Q_s$ ), and sand fraction ( $Q_{sand} > 0.062\text{mm}$ ), at rkm 172  
 1274 given by the discharge- $Q_s$  rating-curve of Sherwood *et al.* (1990). Note that these estimates  
 1275 exclude the sediment contributions of the Willamette and Cowlitz rivers. Also provided are the:  
 1276 (i) Holocene averaged (*ca* last 10,000 yr) estimates of LCR  $Q_s$  conveyed to the lower Columbia  
 1277 River Valley (LCRV; grey rectangle) and amount utilized to fill the LCRV to its present level  
 1278 (blue rectangle); and (ii) estimations of the pre-1900 (black dashed line), 1964 to 1970 (purple  
 1279 line), and post-1980 (pink dashed line) LCR  $Q_s$ . Modified from Sherwood *et al.* (1990).



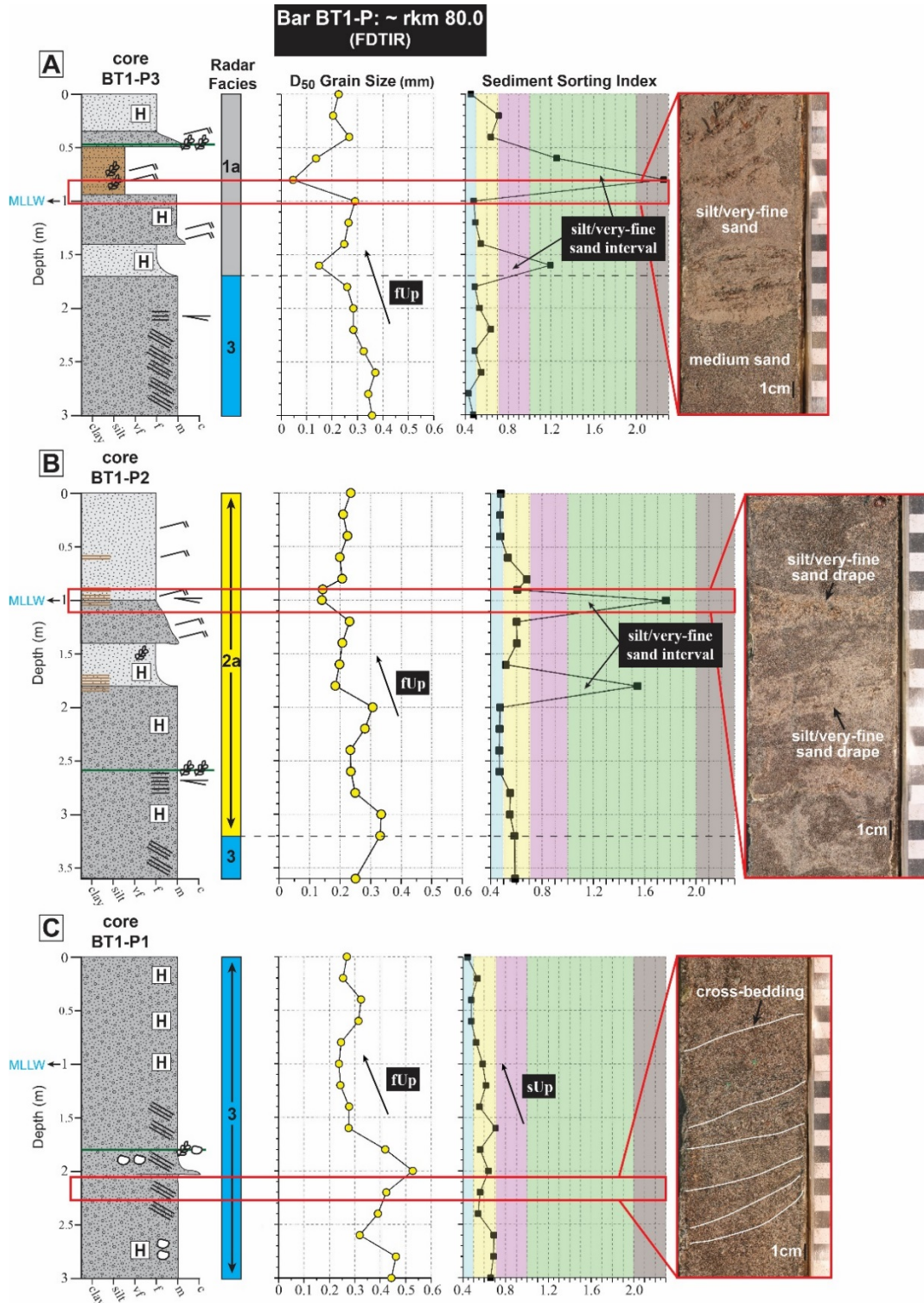
1280

1281 **Figure 6.** (A) to (C) Time sequenced aerial imagery displaying the initial development of Bars  
 1282 BT1-P, CB1-S and CB2-W, in 1990, and their subsequent migration patterns to 2011/2012,  
 1283 relative to GPR-profiles (yellow lines) and vibracores (pink circles) collected in 2011 (Bars BT1-  
 1284 P and CB1-S) and 2013 (Bar CB2-W), respectively. Reported average migration rates were  
 1285 estimated over the time period 1990 to 2011 (Bar BT1-P) and 1990 to 2012 (Bars CB1-S and  
 1286 CB2-W). Note that average migration rates represent the measured straight line distance between  
 1287 the 1990 centre of each bar and its new centre position in 2011, or 2012. Thus, average migration  
 1288 rates are not partitioned into their lateral and longitudinal-oriented components of translation,  
 1289 and represent overall spatio-temporal movement. Lastly, all bars investigated formed within less  
 1290 human affected secondary channels located away from the consistently dredged main navigation  
 1291 channel (see also Fig. 2 for channel and bar locations). Aerial imagery from US National  
 1292 Agriculture Imagery Program (NAIP) at <https://gdg.sc.egov.usda.gov/>.

1293

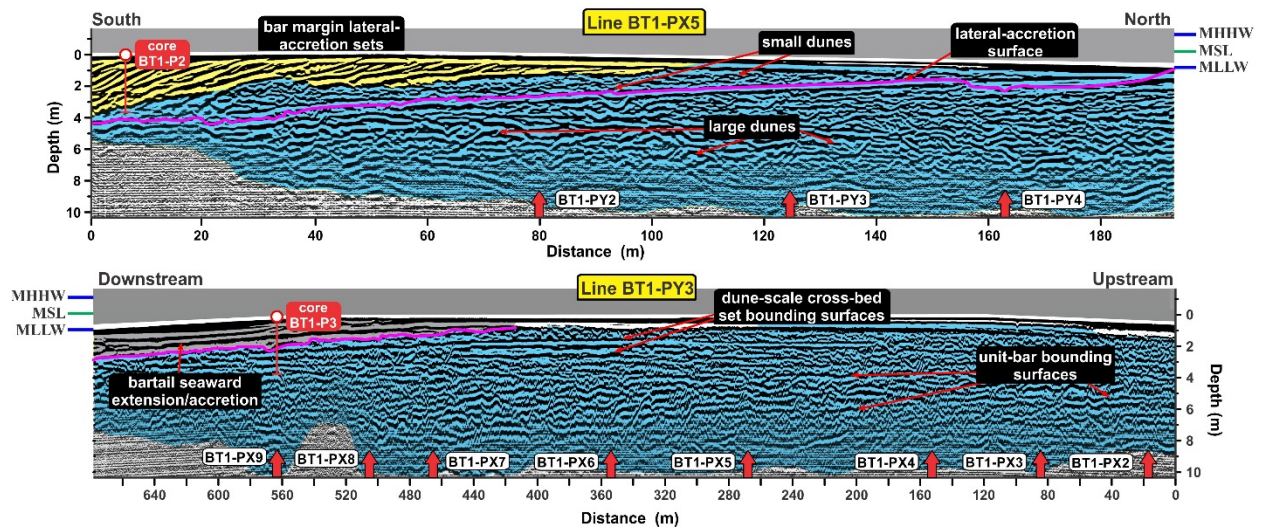
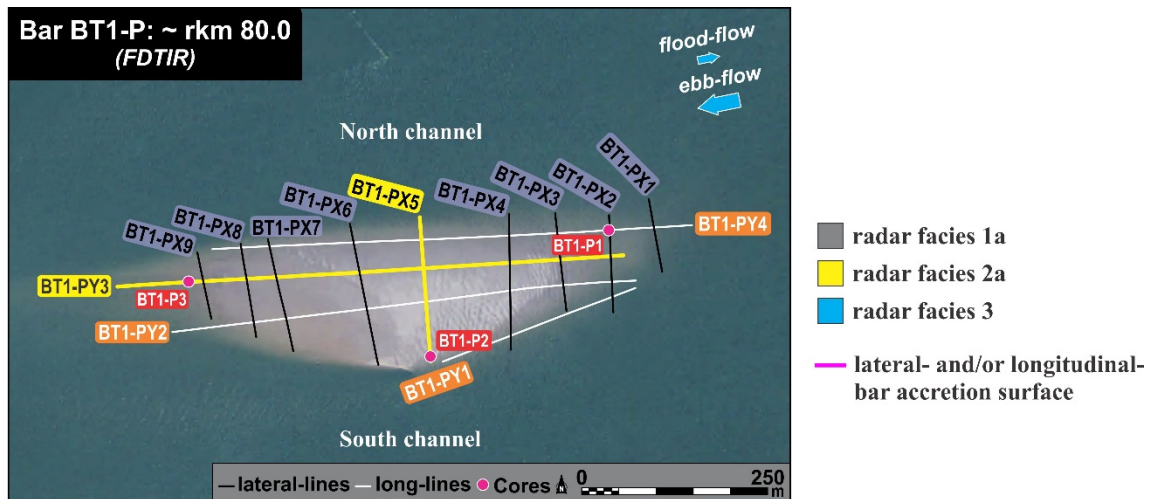
1294

1295



1296

1297 **Figure 7.** Sedimentary logs, and vertical  $D_{50}$  grain size and sediment sorting index trends of the  
 1298 three vibracores collected from Bar BT1-P. Cores are presented from downstream (bartail; core  
 1299 BT1-P3) to upstream (barhead; core BT1-P1). Also marked are the depth intervals that represent  
 1300 the sedimentology and depositional fabric of coupled radar facies. See Table 3 for key to core  
 1301 logs and Fig. 8 for vibracore locations.



1302

1303 **Figure 8.** Interpreted ground penetrating radar (GPR)-profiles from Bar BT1-P positioned within

1304 the fluviually-dominated, tidally-influenced regime (FDTIR). Profiles display the alluvial

1305 architecture of Bar BT1-P as comprising the three major radar facies (1 to 3; colour coded as in

1306 Table 2) identified in this study. Also shown are the locations of vibracores collected along each

1307 profile (cores BT1-P2 and BT1-P3). Note the overall dominance of radar facies 3.

1308

1309

1310

1311

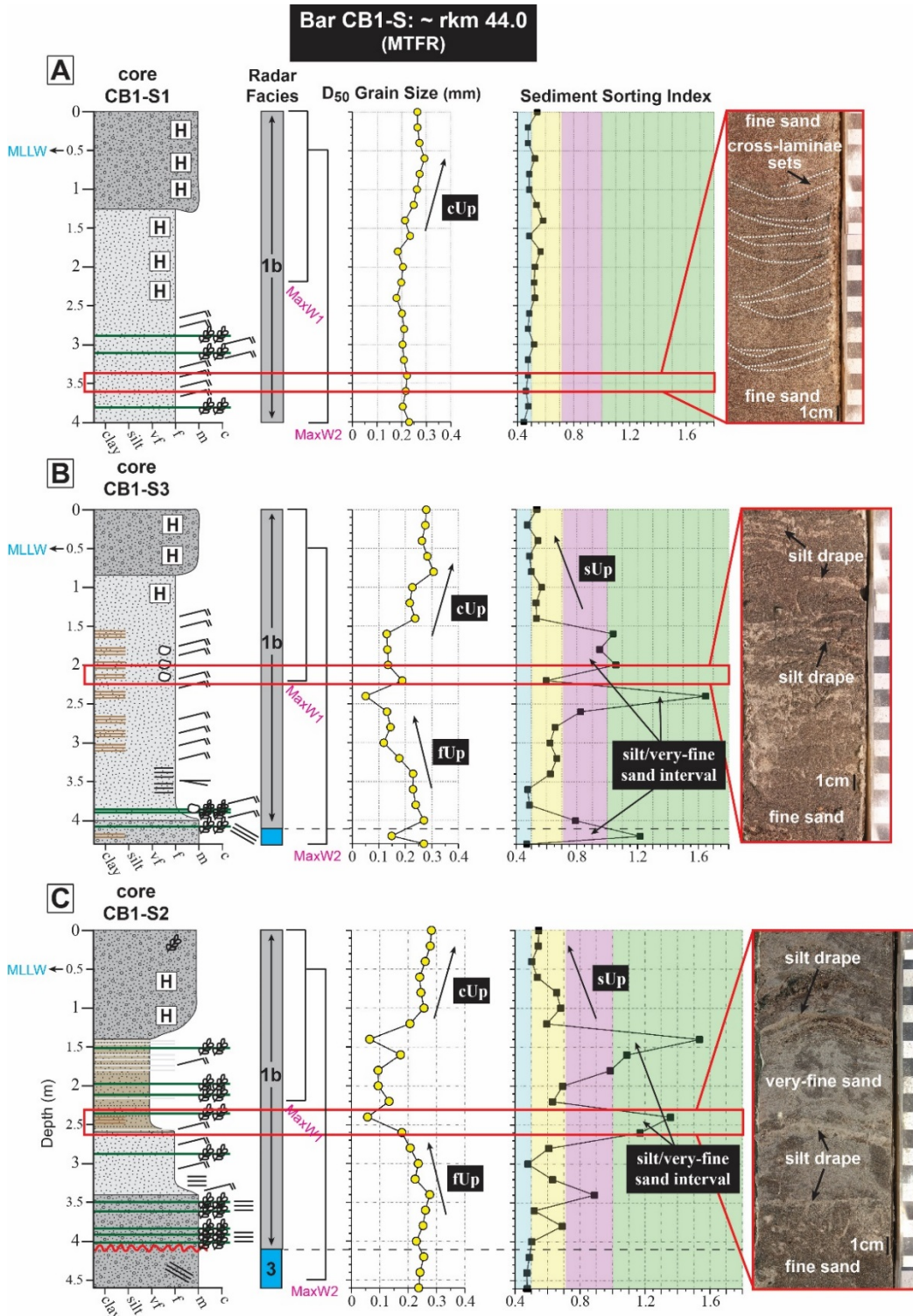
1312

1313

1314

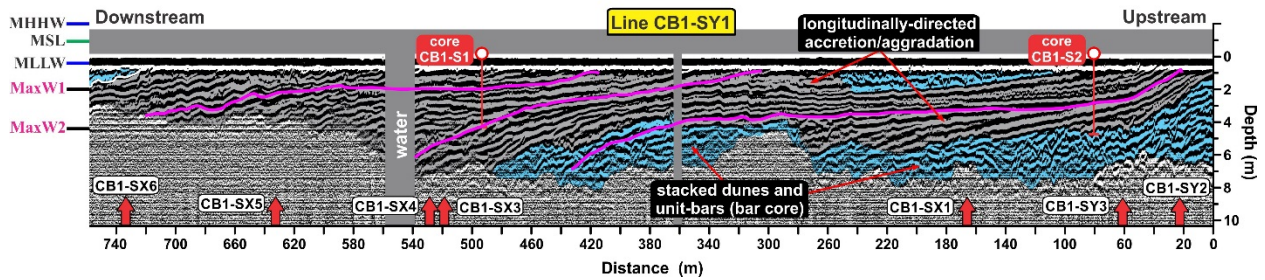
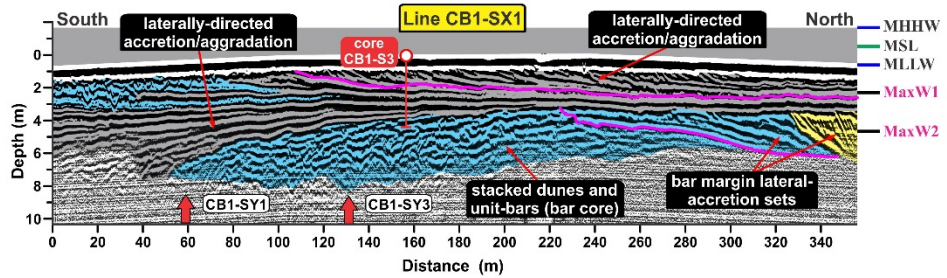
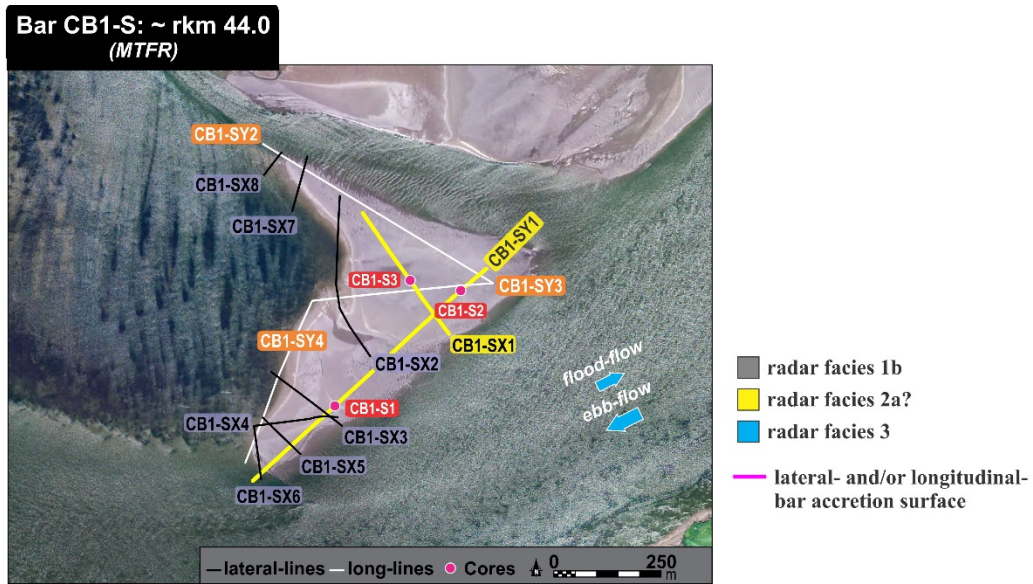
1315

1316



1317

1318 **Figure 9.** Core logs, vertical  $D_{50}$  grain size and sediment sorting index trends of the three  
 1319 vibracores collected from Bar CB1-S. Cores are presented from downstream (bartail; core CB1-  
 1320 S1) to upstream (barhead; core CB1-S2). Demarcated are the depth intervals representing  
 1321 sediments preserved from associated radar facies, and maximum depth windows of potential  
 1322 wind-wave influence. See Table 3 for key to logs and Fig. 10 for vibracore locations.



1323

1324 **Figure 10.** Interpreted GPR-profiles from Bar CB1-S located within the mixed tidal-fluvial  
 1325 regime (MTFR), which display the sedimentary architecture of this bar with respect to preserved  
 1326 radar facies. Also shown are the locations of shallow vibracores collected along each profile  
 1327 (cores CB1-S1, CB1-S2 and CB1-S3), and the colour-coded radar facies. Note the dominant  
 1328 preservation of radar facies 1 and 3.

1329

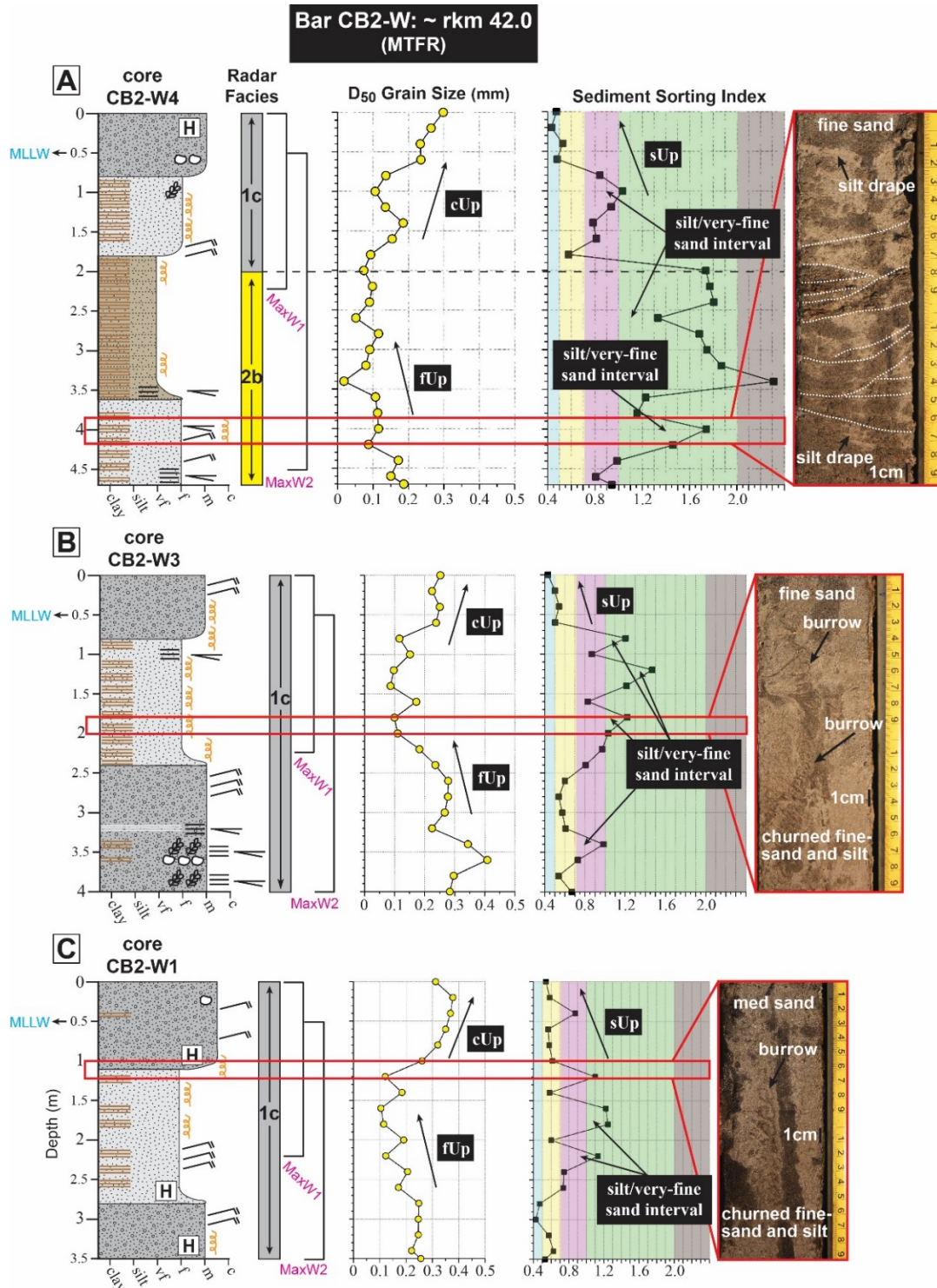
1330

1331

1332

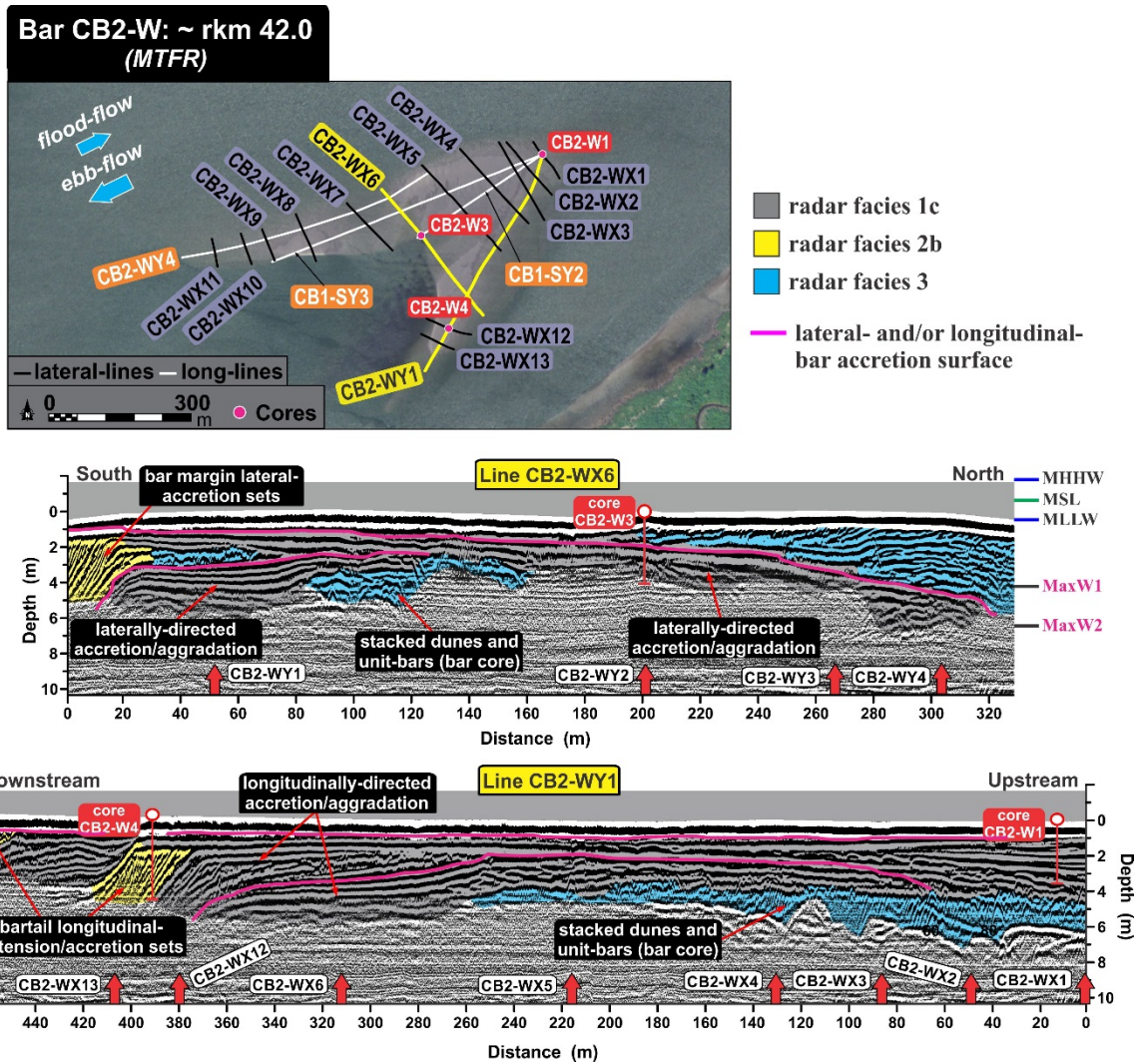
1333

1334



1335

1336 **Figure 11.** Sedimentary logs, vertical  $D_{50}$  grain size and sediment sorting index trends of the  
 1337 three vibracores collected from Bar CB2-W. Cores are presented from downstream (bartail; core  
 1338 CB2-W4) to upstream (barhead; core CB2-W1). Also marked are the depth intervals  
 1339 representing the sedimentology and depositional fabric of coupled radar facies, and maximum  
 1340 depth windows of potential wind-wave influence. See Table 3 for key to logs and Fig. 12 for  
 1341 vibracore locations.



1342

1343 **Figure 12.** Interpreted ground penetrating radar (GPR)-profiles from Bar CB2-W positioned  
 1344 within the mixed tidal–fluvial regime (MTFR). Profiles display the preserved stacking patterns  
 1345 of radar facies within Bar CB2-W. The locations of vibracores collected along each profile  
 1346 (cores CB2-W1, CB2-W3 and CB2-W4) are also shown, together with the colour-coded radar  
 1347 facies. Similar to Bar CB1-S, note the dominant preservation of radar facies 1 and 3.  
 1348

1349

1350

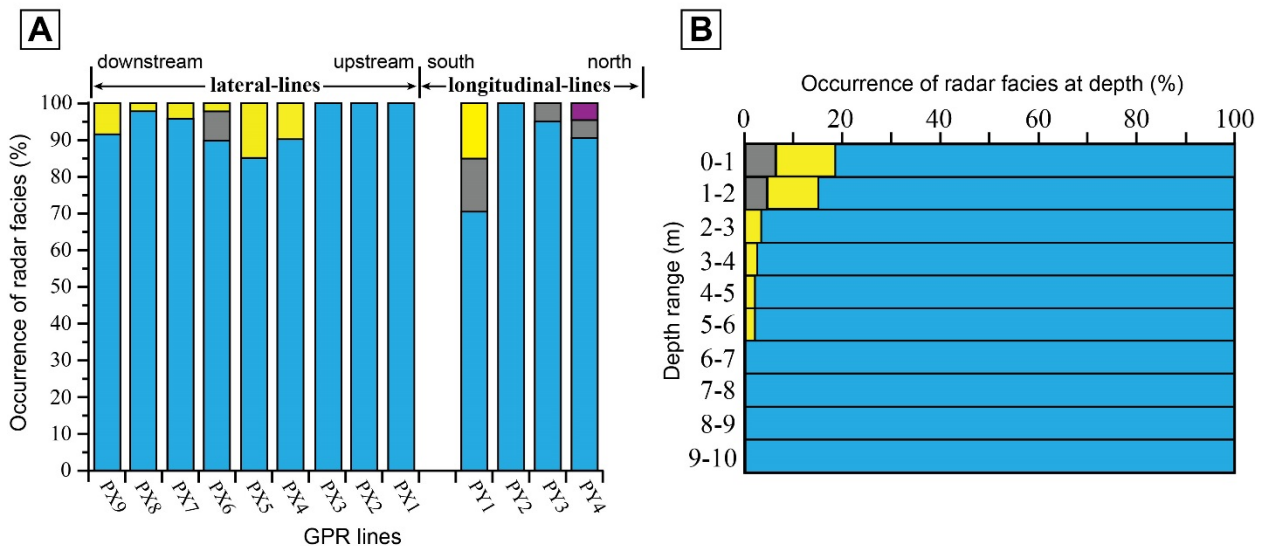
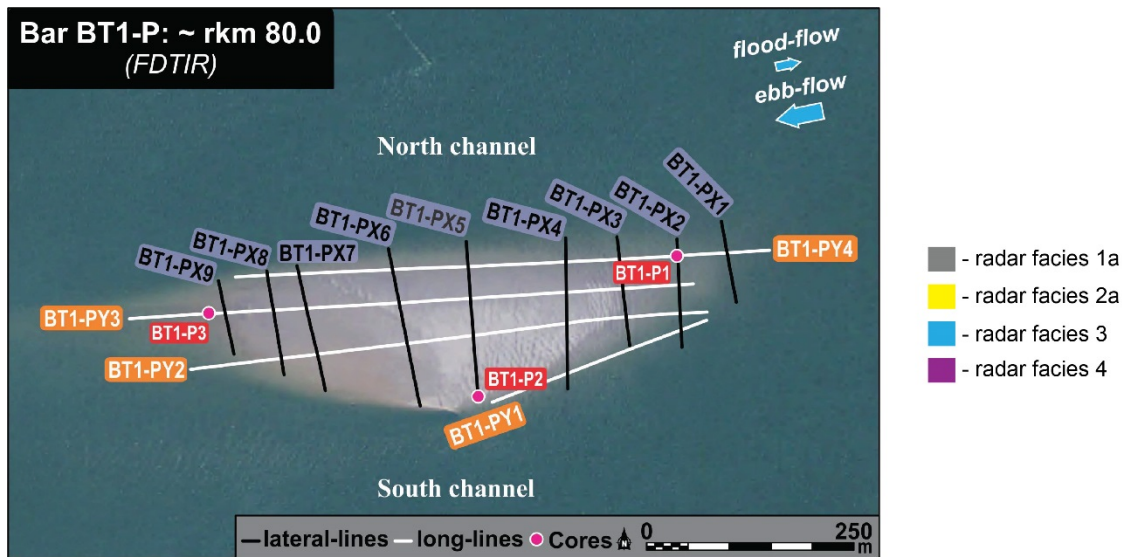
1351

1352

1353

1354

1355



1356

1357 **Figure 13.** (A) Areal occurrences of radar facies within each of the 13 ground penetrating radar  
 1358 (GPR)-transects from Bar BT1-P. This bar is dominated by facies 3 with minimal occurrence of  
 1359 facies 1a and 2a. The occurrence of facies 1a is nearly always constrained to bar-tail  
 1360 downstream-extension (lines PY1, PY3 and PY4), whilst facies 2a is mainly confined to bar-  
 1361 margin lateral-accretion (lines PX4 to PX9). (B) Calculated occurrence of radar facies within Bar  
 1362 BT1-P GPR-transects with respect to depth. Notice the dominance of facies 3 (>80%) throughout  
 1363 all depth intervals.

1364

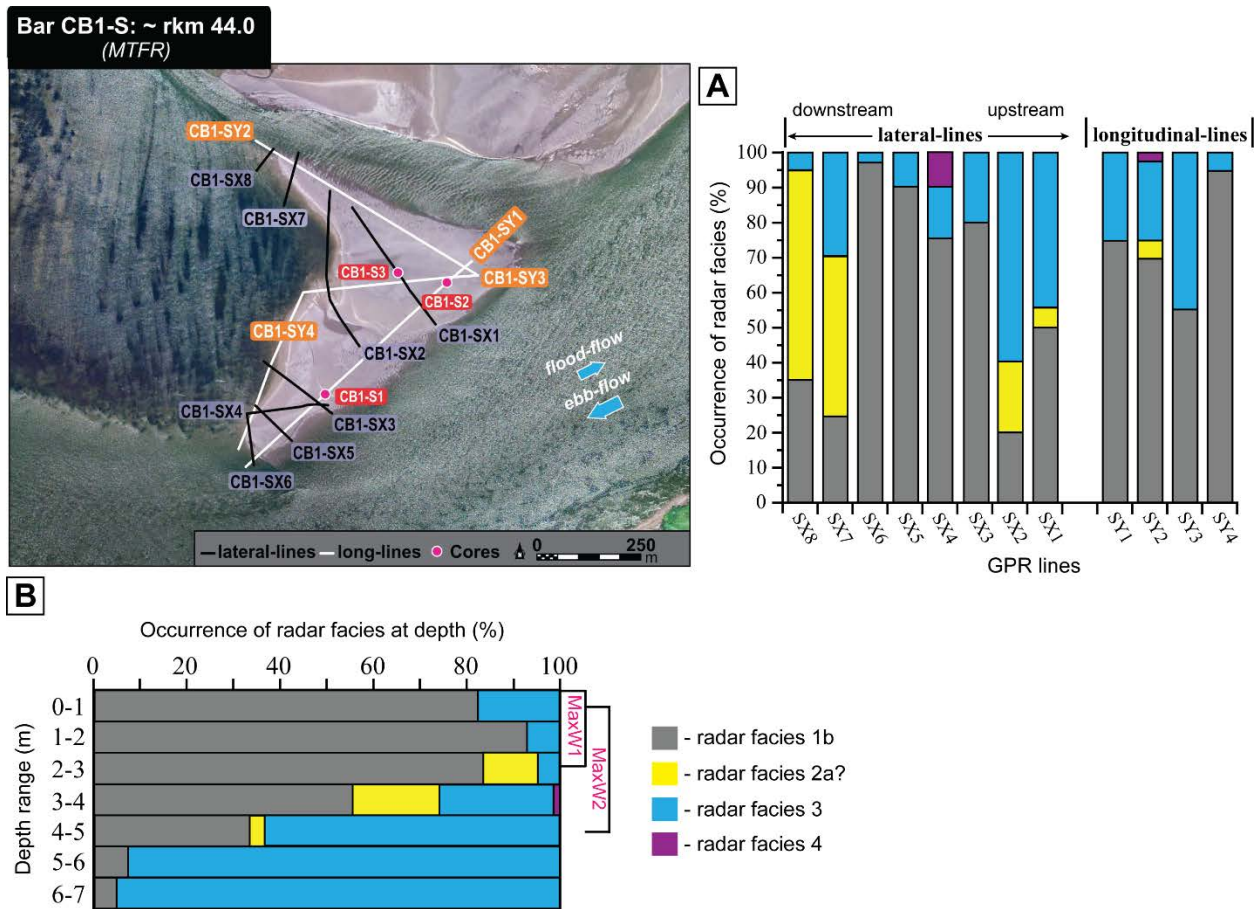
1365

1366

1367

1368

1369



1370

1371 **Figure 14.** (A) Spatial distributions of radar facies areal occurrences within the 12 ground  
 1372 penetrating radar (GPR) profiles at Bar CB1-S. This bar is dominated by facies 1b, with notable  
 1373 occurrence of facies 2a and 3. Preservation of facies 2a is typically restricted to bar-margin  
 1374 lateral-accretion (lines SX1, SX2, SX7 and SX8), whereas facies 3 is found in variable  
 1375 occurrence within all longitudinal and lateral-transsects. (B) Occurrence of Bar CB1-S radar  
 1376 facies with respect to depth. Note that the preservation of facies 3 dominates from 4 to 7 m depth  
 1377 ( $\geq 60\%$ ; below potential wind-wave influence), whilst between 0 to 4 m depth (within potential  
 1378 wind-wave influence) facies 1b ( $\geq 55\%$ ) dominates, as facies 2a and 3 diminish to  $< 25\%$ .

1379

1380

1381

1382

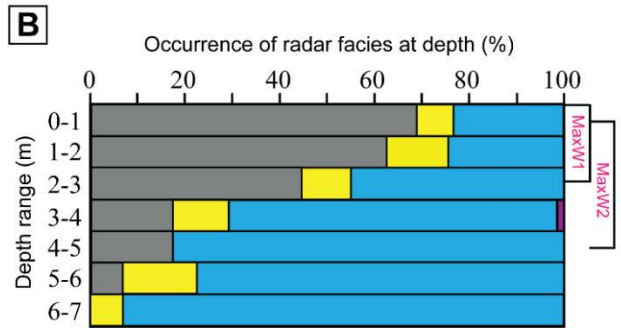
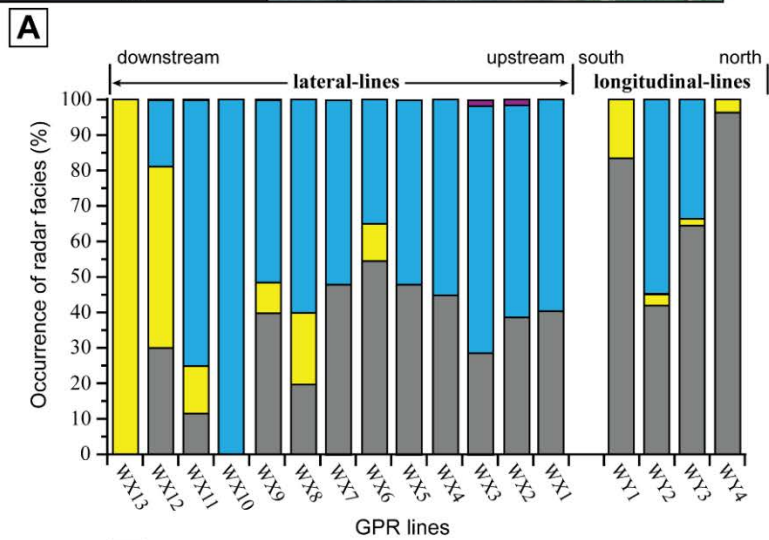
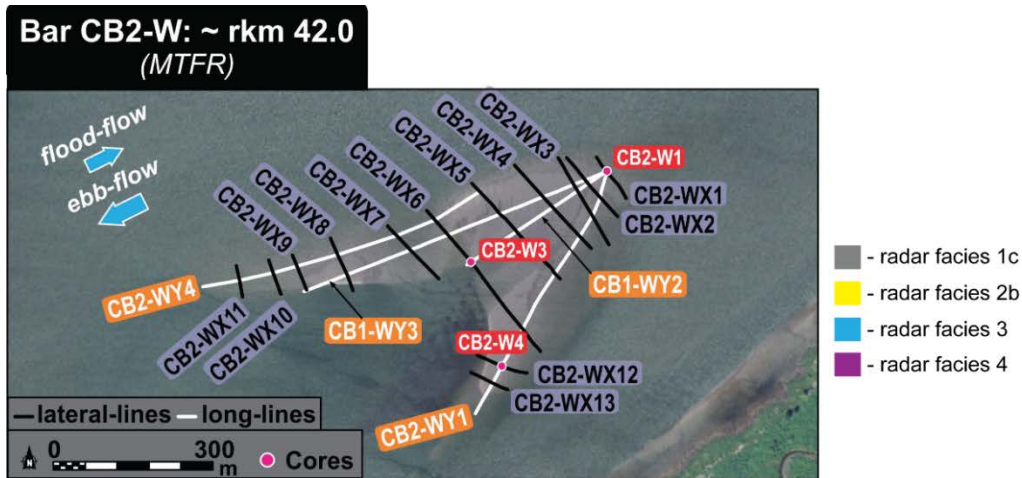
1383

1384

1385

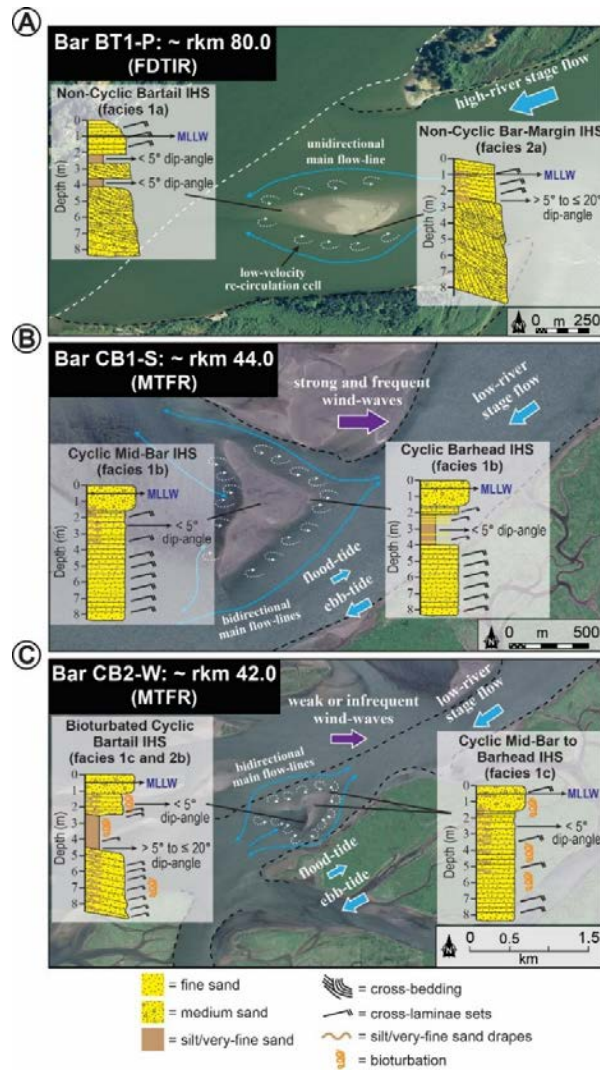
1386

1387



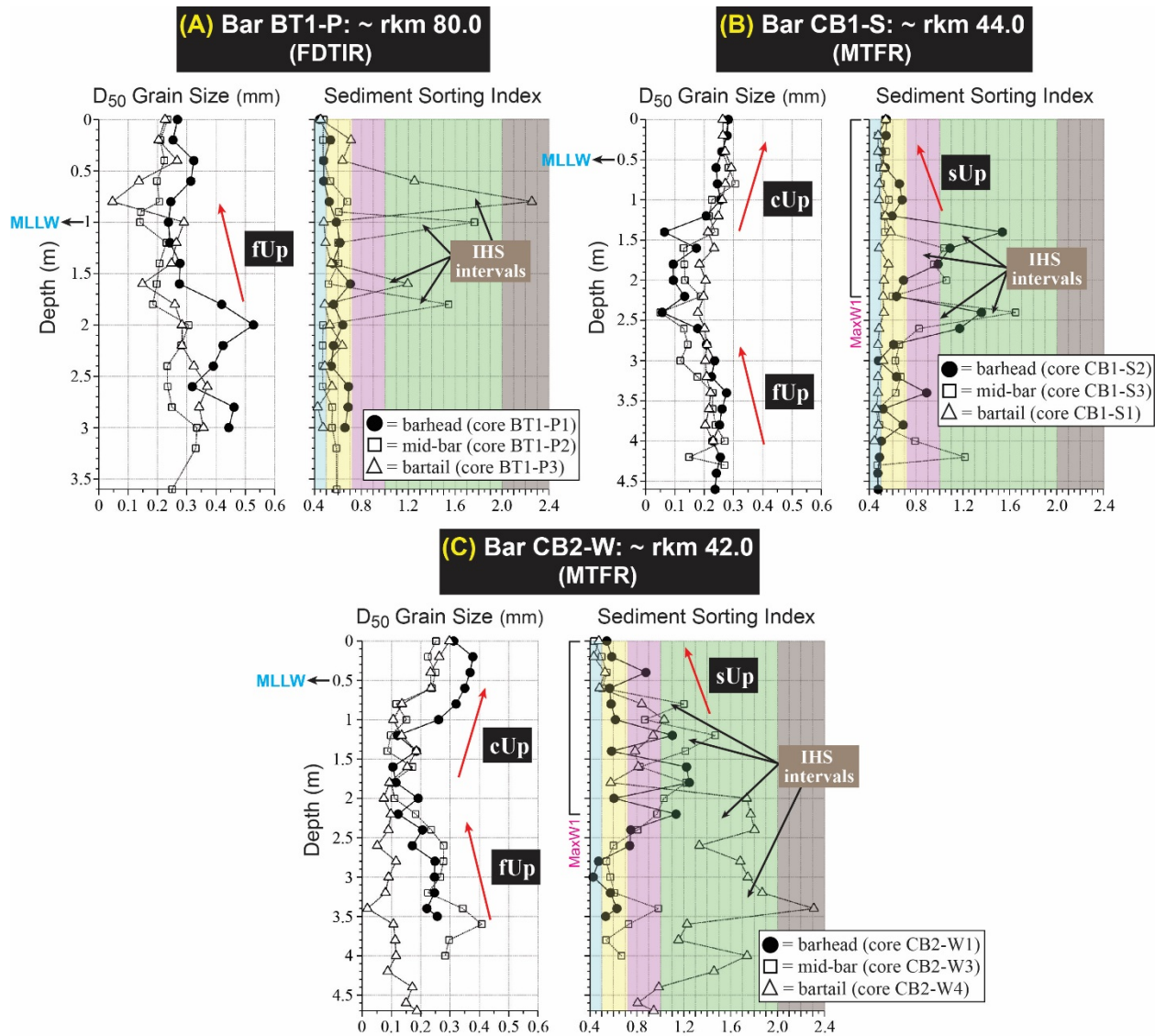
1388

1389 **Figure 15.** (A) Areal occurrence of radar facies within the 17 ground penetrating radar (GPR)  
 1390 transects at Bar CB2-W. This bar primarily comprises facies 1c, 2b and 3, with lower  
 1391 preservation of any style of facies 1 relative to Bar CB1-S. Note that occurrence of facies 2b  
 1392 represents: (i) bar-margin lateral-accretion (lines WX6, WX8, WX9 and WX11-WX13); and (ii)  
 1393 downstream-oriented bartail-limb accretion (lines WY1 and WY4). (B) Occurrences of Bar CB2-  
 1394 W radar facies with respect to depth. Notice also that the preservation of facies 3 dominates from  
 1395 3 to 7 m depth ( $\geq 60\%$ ), whereas between 0 to 2 m depth (within shallowest zone of potential  
 1396 wind-wave influence) facies 1c ( $\geq 60\%$ ) dominates as facies 3 diminishes to  $< 25\%$ . However,  
 1397 unlike Bar CB1-S, facies 2 (in the form of 2b) is more abundant (*ca* 8 to 15% in occurrence)  
 1398 within the 0 to 3 m depth interval.



1400

1401 **Figure 16.** Schematic representations of the different styles, and depositional fabrics and  
 1402 positions, of preserved inclined heterolithic stratification (IHS) within Lower Columbia River  
 1403 (LCR) fluvial-tidal transition (FTT) mid-channel barforms experiencing differing hydraulic  
 1404 processes and sediment transport conditions. (A) IHS is formed primarily during high-river stage  
 1405 events when LCR suspended-sediment concentrations are highest, where fines can be trapped,  
 1406 and deposited, within side-bar and bartail low-velocity recirculation cells. (B) IHS is produced  
 1407 by the redistribution of fines (especially bartail fines) deposited during high-river stage(s) by  
 1408 frequent strong wind-waves and bidirectional tidal-currents at low-river stages. Ebb-tidal  
 1409 currents may carry wind-wave induced resuspended fines downstream, whilst flood-tidal  
 1410 currents and associated slackwater periods may transport and deposit wind-wave induced  
 1411 resuspended fines into mid-bar and barhead accretion-sets. (C) Bartail IHS forms during high-  
 1412 river stage(s) by the same method as (A), but during low-river stage, more infrequent weaker  
 1413 wind-waves do not resuspend as many fines, which allows for IHS production from bartail to  
 1414 barhead that is derived from a combination of high river-stage deposited fines and those  
 1415 deposited during tidal slackwater intervals. Note that all IHS within (C) is bioturbated due to  
 1416 weaker wind-wave energy.



1417  
 1418 **Figure 17.** Plots of barhead to bartail vibracore  $D_{50}$  grain size and sediment sorting trends for the  
 1419 three Lower Columbia River (LCR) mid-channel barforms analysed. (A) Bar BT1-P (fluvially-  
 1420 dominated, tidally-influenced regime – FDTIR) displays a fining-upward trend from its barhead  
 1421 to bartail. (B) Barhead to bartail deposits of Bar CB1-S (mixed tidal–fluvial regime – MTFR)  
 1422 fine-upward then coarsen and sort-upward within MaxW1 at *ca* 1.5 m depth. (C) Bar CB2-W  
 1423 (MTFR) barhead to bartail alluvium fine-upward then coarsen-upward at *ca* 1 m depth, but do  
 1424 not sort-upward until near the top of MaxW1 at *ca* 0.5 m depth. See Table 3 for definitions of  
 1425 abbreviated labels and sediment sorting classifications.

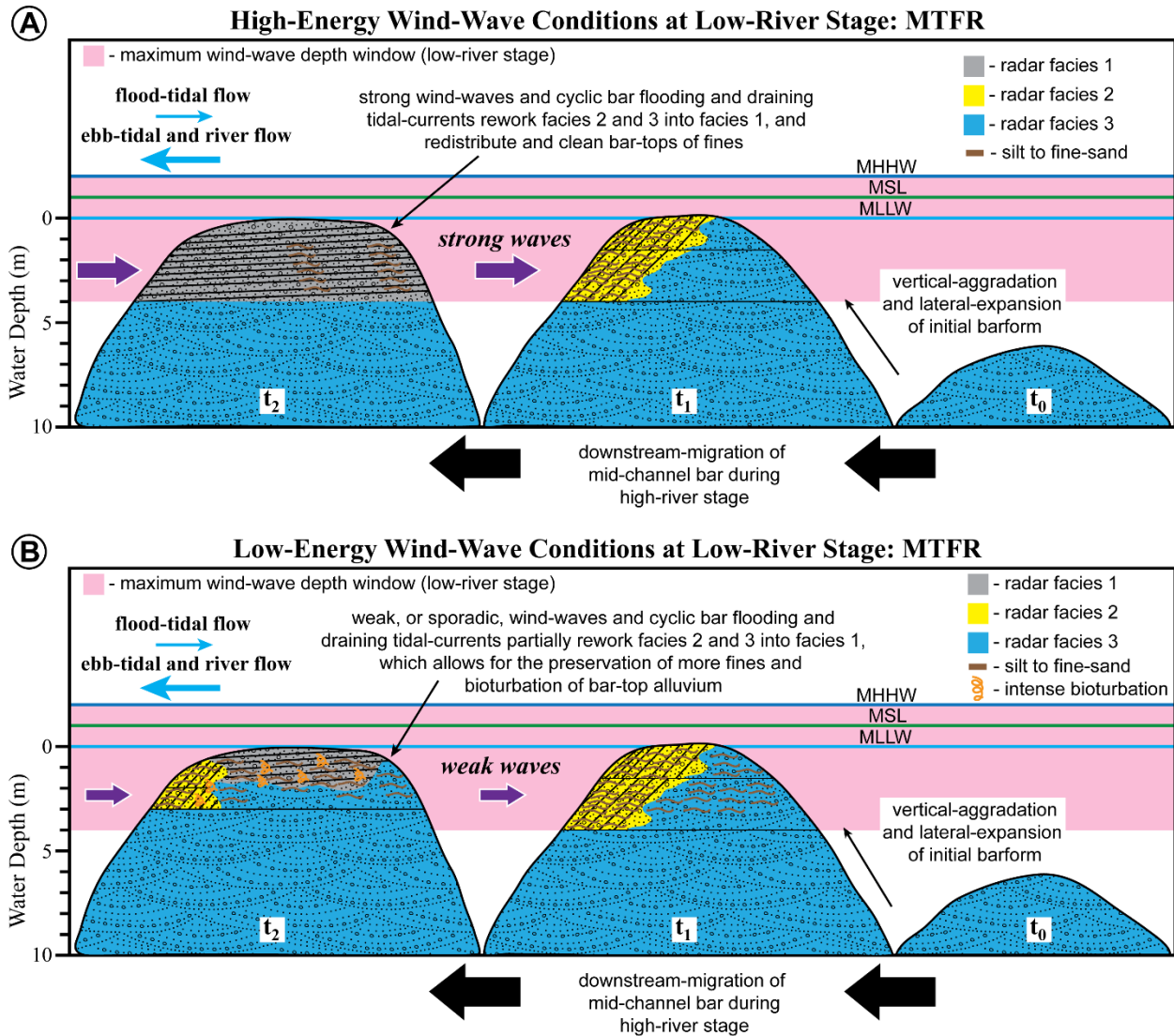
1426

1427

1428

1429

1430



1431

1432 **Figure 18.** (A) Time-sequenced schematic diagram in longitudinal cross-sectional view  
 1433 depicting the architectural and sedimentological evolution of a Lower Columbia River (LCR)  
 1434 barform within the mixed tidal–fluvial regime (MTR) that is affected by frequent and strong  
 1435 intrabasinal wind-waves during low-river stage. (B) Time-sequenced schematic diagram in  
 1436 longitudinal cross-sectional view displaying the architectural and sedimentological evolution of a  
 1437 LCR barform within the MTR that is weakly, or sporadically, influenced by intrabasinal wind-  
 1438 waves during low-river stage.